Near-Horizontal, Two-Phase Flow Patterns of Nitrogen and Hydrogen at Low Mass and Heat Flux

Neil T. Van Dresar
Glenn Research Center, Cleveland, Ohio

James D. Siegwarth
National Institute of Standards and Technology, Boulder, Colorado

Since its founding, NASA has been dedicated to the advancement of aeronautics and space science. The NASA Scientific and Technical Information (STI) Program Office plays a key part in helping NASA maintain this important role.

The NASA STI Program Office is operated by Langley Research Center, the Lead Center for NASA's scientific and technical information. The NASA STI Program Office provides access to the NASA STI Database, the largest collection of aeronautical and space science STI in the world. The Program Office is also NASA's institutional mechanism for disseminating the results of its research and development activities. These results are published by NASA in the NASA STI Report Series, which includes the following report types:

- TECHNICAL PUBLICATION. Reports of completed research or a major significant phase of research that present the results of NASA programs and include extensive data or theoretical analysis. Includes compilations of significant scientific and technical data and information deemed to be of continuing reference value. NASA's counterpart of peer-reviewed formal professional papers but has less stringent limitations on manuscript length and extent of graphic presentations.

- TECHNICAL MEMORANDUM. Scientific and technical findings that are preliminary or of specialized interest, e.g., quick release reports, working papers, and bibliographies that contain minimal annotation. Does not contain extensive analysis.

- CONTRACTOR REPORT. Scientific and technical findings by NASA-sponsored contractors and grantees.

- CONFERENCE PUBLICATION. Collected papers from scientific and technical conferences, symposia, seminars, or other meetings sponsored or cosponsored by NASA.

- SPECIAL PUBLICATION. Scientific, technical, or historical information from NASA programs, projects, and missions, often concerned with subjects having substantial public interest.

- TECHNICAL TRANSLATION. English-language translations of foreign scientific and technical material pertinent to NASA's mission.

Specialized services that complement the STI Program Office's diverse offerings include creating custom thesauri, building customized data bases, organizing and publishing research results . . . even providing videos.

For more information about the NASA STI Program Office, see the following:

- Access the NASA STI Program Home Page at *http://www.sti.nasa.gov*

- E-mail your question via the Internet to help@sti.nasa.gov

- Fax your question to the NASA Access Help Desk at 301–621–0134

- Telephone the NASA Access Help Desk at 301–621–0390

- Write to:
  NASA Access Help Desk
  NASA Center for AeroSpace Information
  7121 Standard Drive
  Hanover, MD 21076

Near-Horizontal, Two-Phase Flow Patterns of Nitrogen and Hydrogen at Low Mass and Heat Flux

Neil T. Van Dresar
Glenn Research Center, Cleveland, Ohio

James D. Siegwarth
National Institute of Standards and Technology, Boulder, Colorado

National Aeronautics and
Space Administration

Glenn Research Center

Acknowledgments

Available from

NASA Center for Aerospace Information
7121 Standard Drive
Hanover, MD 21076

National Technical Information Service
5285 Port Royal Road
Springfield, VA 22100

Available electronically at http://gltrs.grc.nasa.gov/GLTRS

Near-Horizontal, Two-Phase Flow Patterns of Nitrogen and Hydrogen at Low Mass and Heat Flux

Neil T. Van Dresar
National Aeronautics and Space Administration
Glenn Research Center
Cleveland, Ohio 44135

James D. Siegwarth
National Institute of Standards and Technology
Boulder, Colorado 80303

Summary

An experimental apparatus was constructed and operated at the National Institute of Standards and Technology (NIST) to obtain data on the two-phase (liquid and vapor) flow behavior of cryogenic fluids under conditions of low mass and heat flux. The range of flow rates (0.2 to 20 g/s for nitrogen; 0.02 to 0.2 g/s for hydrogen), heat flux (0.07 W/cm^2), and flow-path size (8.7-mm i.d.) were representative of thermodynamic vent systems planned for the pressure control of spacecraft propellant tanks in low gravity. The apparatus was operated in normal gravity with a 1.5° upflow configuration. Numerous tests were conducted with liquid nitrogen and a lesser number with liquid hydrogen. Viewports in the apparatus permitted visual observation of the two-phase flow patterns.

The two-phase flow pattern is a key parameter in understanding and predicting two-phase flow; that is, having proper knowledge of the flow pattern is a critical first step in predicting two-phase flow behavior. In the experiments, various flow patterns were observed and recorded on videotape. The data were used to construct flow pattern maps for each test fluid. Results are presented in the traditional format of a two-dimensional flow pattern map with the liquid and gas superficial velocities used as coordinates.

Computer codes to predict flow patterns were developed from theoretical and/or empirical models reported in the literature. The vast majority of the published modeling work has been validated by a data base that is limited largely to air-water test fluids. Experimental observations were compared with the predicted flow patterns from the computer codes to determine the robustness of the models when applied to cryogenic fluids whose properties can differ significantly from those of air and water. Cryogens also readily evaporate and condense whereas phase change is negligible in air-water flows. This work is a small step in the process of validating models for cryogenic two-phase flow because it is limited to a single angle of inclination, one heat flux, and one tube diameter.

In general, the agreement between the cryogenic experimental results and the analytical predictive methods is reasonably good. Identified in the flow pattern maps are small regions where the models are deficient as a result of phase-change phenomena not accounted for in the analytical models. Certain regions of the maps were beyond the range of the experimental data and could not be completely validated.

Areas that could benefit from further work include modeling of the transition from separated flow, collection of additional data in the bubble and annular flow regimes, and collection of experimental data at other inclination angles, tube diameters, and higher heat fluxes.

Introduction

NASA's Interest

One reason for NASA's interest in cryogenic two-phase flow with low mass and heat flux is the need to design spacecraft heat exchangers used for vaporizing cryogenic propellants. These heat exchangers are a key component of thermodynamic vent systems (TVS) employed to control pressure in unsettled propellant tanks during long-duration space exploration missions.

A unique experimental apparatus was built at the National Institute of Standards and Technology in Boulder, Colorado, under a joint research effort with the NASA Lewis (now Glenn) Research Center to study the two-phase flow of cryogenic nitrogen and hydrogen under conditions of low mass and heat flux. This report describes the apparatus and presents a comparison of the observed two-phase flow patterns and the analytical predictions developed from models primarily validated with air-water data.

This work is considered precursor to follow-on experiments at other angles of inclination, tube diameters, and heat fluxes. Because it is ultimately desired to conduct experiments in low gravity, this work is expected to guide the development of these normal- and low-gravity experiments.

Two-Phase Flow Overview

The two-phase flow of cryogens is a complex interaction of energy and momentum transfer. Flow with heating is characterized by a phase change from liquid to vapor in the flow

direction. Normal flow boiling is initiated when the tube wall temperature sufficiently exceeds the bulk fluid temperature and vapor bubbles nucleate at the wall. Boiling may be either subcooled or saturated, depending on local liquid conditions. Prior to nucleation, liquid may become superheated by several degrees and then cool to saturated conditions once vapor is present. In the TVS, phase change first occurs as the flow expands through a Joule-Thomson device. At low heat flux, further phase change may occur at existing liquid-vapor interfaces rather than at nucleation sites on the wall.

With further heating of the two-phase fluid, additional change from liquid to vapor phase increases the quality and void fraction as the flow proceeds downstream. For a sufficiently long tube, the two-phase flow consists of different flow patterns as the vapor quality changes from zero near the inlet to unity near the outlet. Various flow patterns will exist at different downstream positions in the tube. A typical flow pattern sequence in a horizontal evaporator tube might be as follows: Initially, the fluid is predominantly liquid with nucleate boiling at the wall creating bubbles that are entrained in the flow; this is bubbly flow. As more vapor is produced, the bubbles coalesce to form larger vapor regions, and plug or slug flow exists. Production of still more vapor leads to high vapor velocity and transition to wavy and annular flows. Beyond this point, the wall dries out, leading to mist flow and then single-phase vapor flow.

If each phase has a characteristic velocity, the slip, or velocity ratio, depends upon void fraction, quality, and fluid densities as follows:

$$\frac{u_g}{u_f} = \left(\frac{x}{1-x}\right)\left(\frac{\rho_f}{\rho_g}\right)\left(\frac{1-\alpha}{\alpha}\right) \qquad (1)$$

where u_g and u_f are the saturated vapor and saturated liquid velocities, respectively; x is the quality at thermodynamic equilibrium; ρ_f and ρ_g are the saturated liquid and saturated vapor densities, respectively; and α is the void fraction. The slip ratio may be approximately equal to one for dispersed bubble or mist flows. Generally, it is not equal to one and therefore void fraction and quality must be independently measured.

As one would expect, the heat transfer characteristics of two-phase flow change with flow pattern. In general, heat transfer coefficients are higher when the wall is wetted and when the flow is undergoing vigorous mixing. Wall temperatures in the vicinity of the inlet can be expected to increase until nucleation begins. Temperatures will then decrease as bulk boiling occurs until the wall dryout point is reached. At this point, a sudden increase in wall temperature is seen as a result of much lower heat transfer coefficients.

Analytical modeling of such complex flow patterns is difficult. Models of differing levels of complexity have been developed. The simplest is the homogenous model that uses average values for fluid properties and flow parameters. More complete models, for which separate equations are written for each phase and are sometimes extended in second and third dimensions, require experimental determination of a larger number of unknown constants. One approach that can be employed is to use a homogeneous-flow model for bubbly flows without slip, a separated-flow model for annular and stratified flows, and a drift flux model for bubbly flow with slip and intermittent (slug and plug) flows.

Flow Pattern Overview

The topology of two-phase flow has a major effect on heat transfer and pressure drop in the flow channel. In two-phase flow modeling, the first step is generally to predict the proper flow pattern. This is analogous to calculating the Reynolds number for classification of a single-phase flow as laminar or turbulent. Characteristics of common flow patterns found in horizontal flow and normal gravity are discussed in the following sections. The descriptions are summarized from several textbooks on two-phase flow (refs. 1 and 2).

Bubble flow.—Vapor is distributed as discrete bubbles in a continuous liquid phase. Bubbles are small and approximately spherical and tend to travel in the upper portion of the tube because of the effect of gravity.

Plug flow.—Bubble length may vary considerably. The nose of the bubble has a spherical cap and the bubble travels in the upper part of the tube.

Stratified flow.—Each phase flows separately with a relatively smooth interface. Liquid, having a higher density, flows along the bottom part of the tube.

Wavy flow.—Similar to stratified flow except the interface is disturbed by waves traveling in the direction of flow.

Slug flow.—High gas velocity causes waves to be picked up in a slug. The slug is aerated and contains bubbles. Slug flow is faster and more chaotic than plug flow and has less interface definition.

Annular flow.—A high-velocity-gas core is surrounded by a liquid film. The film is thickest on the bottom and may not extend completely around the periphery of the tube.

Mist flow.—Discrete liquid droplets are entrained in a high-velocity gas flow. The tube wall is dry.

Generally, flow patterns for slight angles of inclination are nearly the same as those for horizontal flow. Separated flows such as stratified and wavy disappear for upward inclinations of more than a few degrees and are not observed in vertical flow or in the low-gravity environment.

Flow pattern data have historically been presented in a graphical format known as a flow pattern map. The first flow pattern map for horizontal flow was developed by Baker (ref. 3) for the petrochemical industry. The Baker map is plotted as a function of the vapor and liquid superficial mass velocities combined with fluid property groups. Since it is not dimensionless, the Baker map is not general. A common practice has been to plot flow pattern maps as functions of the gas and liquid

superficial velocities (velocities of each phase if it alone were traveling in the tube).

Flow patterns have been extensively mapped experimentally for common fluids such as air-water and to a lesser extent, steam-water. Openly published data for cryogens are severely limited in availability. Properties of cryogenic fluids differ substantially from those of ordinary fluids and include a greater propensity to vaporize. This work presents experimental results for a single inclination angle and diameter of the tube and compares them with predictions from general models for two-phase flow mapping applied to cryogenic fluids.

The appendix lists video clips of selected flow pattern samples stored on the compact disk that accompanies this report.

Symbols

A cross-sectional area of flow path, m^2

$\tilde{A}$ dimensionless cross-sectional area of flow

Bo Bond number

C coefficient for Blasius friction factor

$\mathcal{C}_2$ coefficient from wave stability criteria

c_p specific heat at constant pressure, J/g-K

D pipe inside diameter, m

$\mathcal{D}$ hydraulic diameter, m

$\tilde{\mathcal{D}}$ dimensionless hydraulic diameter

d_C dispersed bubble diameter, m

d_{CB} critical bubble diameter for creaming, m

d_{CD} critical bubble diameter for coalescence, m

F modified Froude number

g acceleration due to gravity, m/s^2

H total enthalpy flow, J/s

h specific enthalpy, J/kg

ℓ liquid level in stratified flow, m

$\tilde{\ell}$ dimensionless liquid level in stratified flow

i electrical current, A

j summation index for wall or volume segment number

k summation index for wall material

m mass, kg

$\dot{m}$ mass flow rate, kg/s

n Blasius friction-factor exponent

P pressure, kPa

dP/dx pressure gradient, kPa/m

$\dot{Q}$ rate of heat input, W

Re Reynolds number

$\tilde{S}$ dimensionless wetted perimeter

$\tilde{S}_i$ dimensionless liquid-gas interface length

T temperature, K

t time, min

u velocity, m/s

$\tilde{u}$ dimensionless velocity

$\mathcal{U}$ total internal energy, J

u specific internal energy, J/kg

V voltage, V

$\mathcal{V}$ volume, m^3

$\dot{\mathcal{V}}$ volumetric flow rate, m^3/s

X^2 Martinelli parameter

x quality at thermodynamic equilibrium

Y inclination parameter

α void fraction

β angle of inclination from horizontal (upward is positive), deg

δ film thickness in annular flow, m

δ^* dimensionless film thickness in annular flow

κ	rate of energy dispersion per unit mass, m^2/s^3
ν	kinematic viscosity, m^2/s
ρ	density, kg/m^3
$\partial\rho/\partial P$	density gradient with respect to pressure, kg/m^3-kPa
σ	surface tension, N/m
τ	shear stress, N/m^2

Subscripts:

f	saturated liquid
final	final (end of test)
G	gas
g	saturated vapor
i	interfacial
in	inlet
init	initial (start of test)
L	liquid
lk	due to heat leak
m	mixture
out	outlet
ph	preheater
RA	resistor in series with preheater
RB	resistor in series with test section
sat	saturated conditions
tot	total
tp	two-phase fluid
ts	test section
w	wall
1	bellows
2	downstream

Superscript:

s	superficial

Apparatus

Overview

The apparatus constructed for this experiment had a short test section with an upstream heating source used to set the inlet thermodynamic condition. Viewports at each end of the test section permitted flow observations. This design approach enabled data collection over a range of fluid quality from zero to unity while visual information about the flow was obtained. The downside to this approach is that inlet conditions at the test section may not be completely representative of local conditions in a long tube where the flow undergoes a continuous change from single-phase liquid to single-phase gas. Since flow patterns are highly dependent on the upstream history of the flow, the hydrodynamics and heat transfer processes in this apparatus may have differed from those in a long evaporator tube or heat exchanger.

Figure 1 is a simplified schematic diagram of the two-phase flow apparatus. The major components identified in the figure are the liquid supply Dewar, bellows, stepper motor drive system, vacuum jacket, radiation shield, preheater, test section inlet, viewports, heated test section, parallel-flow heat exchanger, liquid separator, and backpressure regulator. The majority of the flow path for the test fluid was 9.5-mm-outside-diameter tubing. Short lengths of copper tubing were used at temperature measurement points; otherwise, the flow-path material was stainless steel to reduce axial heat conduction. Upon exiting the bellows, the liquid rose vertically through the Dewar and lid. This section was 12.7-mm-outside-diameter tubing. After clearing the top of the Dewar lid, the flow path was nearly horizontal until the liquid separator was reached. Vapor exiting the apparatus was vented to the atmosphere through a backpressure regulator.

During initial testing, the flow path was horizontal after clearing the top of the Dewar. With this orientation, nitrogen vapor bubbles would frequently travel upstream against the flow during or after bubble development. It was apparent that prohibitively long times would be necessary to establish quasi-steady conditions for the experiment and that these conditions could be oscillatory in nature. It was decided to modify the apparatus to produce a slight upward slope in the flow path. The data reported herein were obtained with a flow path having a 1.5° slope from horizontal. In this configuration, bubbles would preferentially travel in the downstream direction, and steady conditions could be readily established and maintained during experiments.

The vertical rise from the bellows exit to the elbow above the Dewar lid was 1.3 m. The preheater inlet was located very
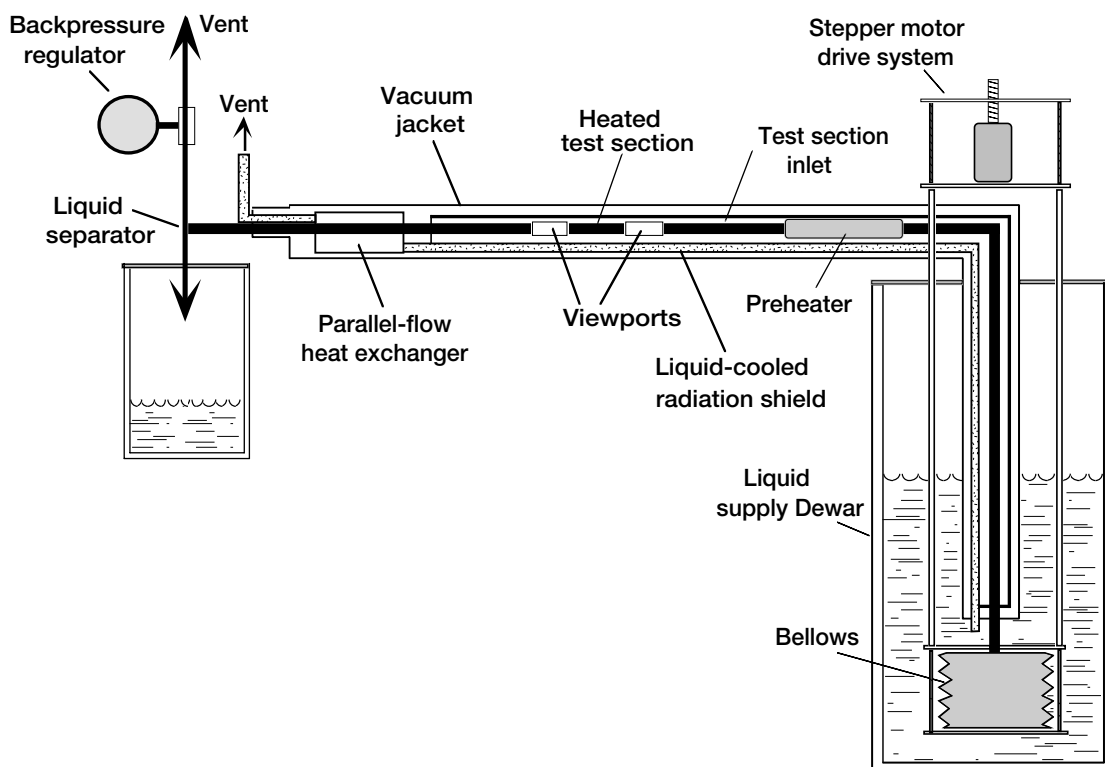
Figure 1.—Cryogenic two-phase test apparatus (not to scale).

near the elbow and was 2.7 m from the preheater inlet to the midpoint of the test section. The inclined flow path was approximately 5.7 m long and had a vertical rise of 15 cm.

Components

Liquid supply Dewar.—Fluid for each experimental run was supplied by an 89-liter steel Dewar that had an outer jacket filled with liquid nitrogen. The fiberglass neck of the Dewar reduced heat conduction from the lid assembly, and four horizontal copper radiation shields suspended below the lid further reduced heat leak from the lid. The lid penetrations include three pull rods, instrumentation feedthroughs (for the capacitance probe, liquid-level point sensor, and bellows pressure), a shaft connected to the bellows shutoff valve, a fill line, a vacuum-jacketed vent line, and the vacuum-jacketed line for liquid outflow. The Dewar was equipped with a capacitance probe to measure liquid level and a point sensor positioned at the maximum fill level. The Dewar lid was bolted to a rigid frame and supported the Dewar and stepper motor drive system. The Dewar could be lowered into a pit by a cable winch to gain access to the internal hardware.

Bellows.—A bellows available from an earlier project (ref. 4) was submerged in the bottom of the Dewar and drove the fluid flow. The bellows served as the flow-metering device, providing a constant volumetric flow rate of liquid as set by the stepper motor drive speed. The bellows was fabricated from a stack of stainless steel washers with alternating inside and outside edges of adjacent washers welded together. The top plate of the bellows was stationary while the bottom traveled. The bellows had an outside diameter of 24.1 cm and a maximum stroke of 24 cm. In this work, the stroke was limited to approximately 19 cm. A pressure tap in the top plate permitted measurement of the internal bellows pressure. A fill valve allowed the bellows to be filled with liquid. The valve was closed during testing.

Stepper motor drive system.—The bellows was compressed by a stepper motor and drive screw mounted on top of the supply Dewar lid. The drive screw moved a yoke attached to the bellows by three pull rods. The motor position was controlled to a resolution of 25 000 steps per revolution of the drive shaft. Motor speeds ranged from 0.001 to 0.1 revolutions per second (rps). Limit switches at the top and bottom ends of the travel range of the yoke automatically stopped the motor to prevent damage to the motor or bellows. A flex coupling installed between the motor and drive screw provided overload protection.

Vacuum jacket.—The test fluid flow path from the bellows to the parallel-flow heat exchanger was enclosed in a vacuum jacket built from stainless steel vacuum components equipped with ISO flanges. The components had diameters of either 10.2 or 15.2 cm. Two 29.5-cm glass sections of the vacuum jacket were located at positions that allowed visual observation through the viewports described below. The top and bottom of these sections were fitted with aluminum circular cylinder

shields. The gaps between the top and bottom aluminum shields formed two 29.5- by 6.4-cm strips for seeing the viewports. A portable air-cooled diffusion pump connected to the jacket maintained a typical vacuum level of 10^{-4} to 10^{-5} Pa.

Radiation shield.—A 4.4-cm-diameter copper radiation shield surrounded the flow path from inside the supply Dewar to the parallel-flow heat exchanger. In the vicinity of the test section, the shield was U-shaped with a removable flat top to allow access to the test section. A 9.5-mm-diameter copper tube was soldered to the shield along its entire length. This tube contained a cooling flow of liquid from the supply Dewar to maintain the shield at a temperature equal to that of the test fluid, thus essentially eliminating radiative heat transfer to the test fluid from the surroundings. The flow through the cooling tube was drawn from liquid in the supply Dewar (outside the bellows) by a portable vacuum pump. A coiled-tube heat exchanger exposed to ambient conditions vaporized and warmed the cooling flow before it entered the pump. A thermocouple placed near the downstream end of the shield allowed monitoring of the cooling flow discharge temperature. The flow was regulated manually by a hand valve to maintain an adequate flow rate through the radiation shield. Small (1.9- by 5.1-cm) cutouts in the radiation shield allowed viewing of the viewports. At the cutout locations, a glass tube was clamped inside the shield. Since the glass was kept cold and was radiatively opaque, radiation heat transfer through the cutouts was minimized.

Preheater.—The function of the preheater was to alter the thermodynamic state of the subcooled liquid flow from the bellows. Heat was added to bring the fluid to a two-phase liquid and gas state. It consisted of a 64-cm-long, thin-walled stainless steel shell that housed a 750-W heating element. The test fluid entered and exited the preheater via the 9.5-mm-diameter inlet and outlet at opposing ends of the shell. A cross section of the preheater is shown in figure 2. Note that the heating element occupied the lower region of the shell volume. This feature minimized prolonged contact of vapor with the heating element in that the vapor bubbles rose to the top of the shell and then exited the preheater with minimal superheating.

Test section inlet.—The inlet to the test section was a 9.5-mm-outside-diameter copper tube (15 cm long) with an attached silicon diode temperature sensor. The high thermal conductivity of the copper tube allowed measurement of the average inlet wall temperature. Since this section was isothermal, its temperature was equal to the temperature of the fluid at this location. This temperature was considered to be the bulk temperature of the fluid as it entered the test section.

Viewports.—Viewports located upstream and downstream of the test section were made of glass tube segments about 3.2 cm long and had inside diameters approximately the same as those of the test section. The viewports were handcrafted by a glassblower and had Kovar tubes fused into each end. The Kovar tubes were soldered to stainless steel tubing. Detailed measurements of the inside diameters revealed that the

windows are slightly larger at 9.3 mm whereas the glass-to-metal seals have a slight neck to about 7.7 to 8.3 mm in diameter.

Test section.—The test section was an electrically heated brass tube (66.5 percent copper, 33.0 percent zinc, 0.5 percent lead). It was 26 cm long and had an outer diameter of 12.5 mm. It was bored to an inner diameter of 8.74 mm. After completion of the test series, the internal roughness of the test section was measured at six locations. Roughness measurements ranged from 2 to 4 μm. On the outside, 0.508-mm-deep grooves with 14.2 turns per centimeter were machined into the surface. The heating element, a high-resistance, insulated nickel alloy wire, was wound in the grooves and secured with a liberal coating of varnish applied during the winding. The resistance of the wire was 105 Ω/m and the total length was calculated to be about 13.8 m, giving a total resistance of 1450 Ω. The high resistance allowed the use of microampere currents, which generated negligible heating in the attached current leads. At the test section midsection and at each end, copper clamp assemblies were attached. Each clamp served as a mounting surface for two silicon diode temperature sensors that were secured by varnish. A flattened insulated copper wire was wound in the grooves (on top of the heating wire) to thermally shield the clamps from the heating element. The clamp dimensions are given in figure 3, and the overall arrangement of the test section, heating element, temperature sensor clamps, and viewports is shown in figure 4.

Parallel-flow heat exchanger.—Downstream of the test section, the cooling flow of the radiation shield was used to intercept heat conduction along the main flow path from the downstream end. This was accomplished through the use of a concentric-tube heat exchanger. The annulus was filled with cold fluid from the radiation shield cooling flow that flowed
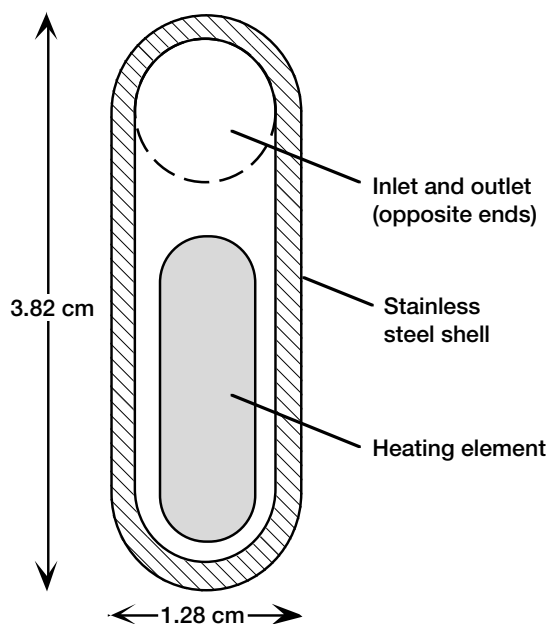

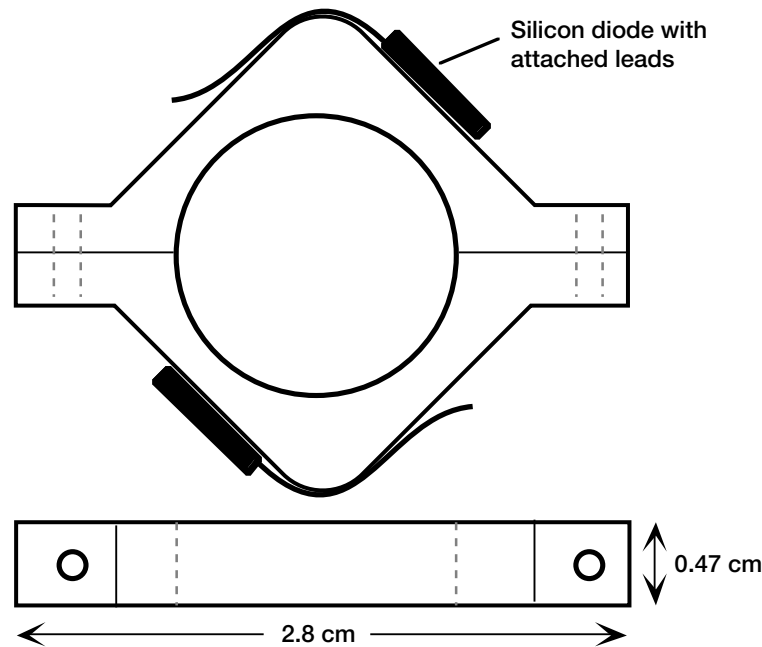Figure 2.—Cross-sectional view of preheater.

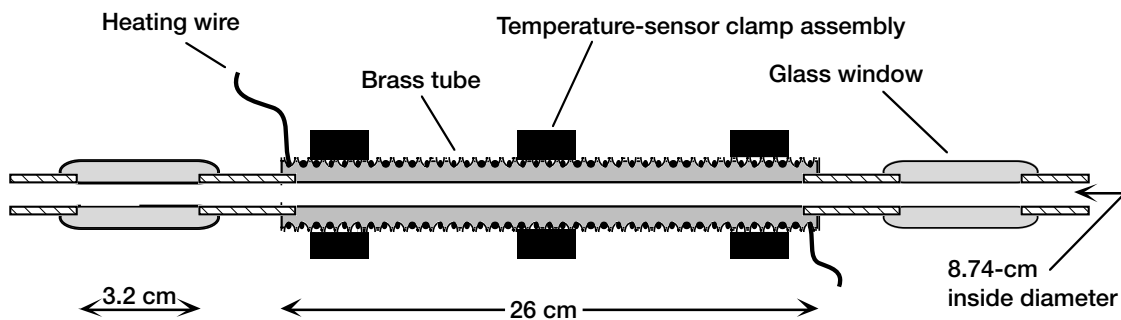Figure 3.—Test section temperature-sensor clamp assembly.

Figure 4.—Complete test section assembly (not to scale).

parallel to the test fluid leaving the test section. The exchanger was constructed of copper and stainless steel tubing and copper plumbing fittings.

Liquid separator.—Initially, the apparatus had no liquid separator and all the two-phase flow was directly vented to the atmosphere. Early on in preliminary testing, it became apparent that vaporization of liquid in the vent line was producing pressure disturbances of a substantially larger magnitude than those in the remainder of the apparatus. These disturbances would regularly reverse the flow direction, and large vapor bubbles would travel upstream through the system. Under these unsteady conditions, meaningful data would be difficult if not impossible to obtain. Therefore, a liquid separator was added to the apparatus. The separator was simply a vertically oriented T-section in the downstream end of the flow path. When the flow encountered the T, vapor preferentially flowed upward to the vent. Meanwhile, liquid dropped downward at the T-section into a receiver Dewar where it accumulated. As liquid in the

receiver Dewar vaporized, the generated gas was free to rise through the T-section and flow to the vent.

Backpressure regulator.—A backpressure regulator attached to the vent system maintained quasi-steady pressures during experiments. A backpressure of 14 to 28 kPa was generally used. This range allowed sufficient subcooling of the test fluid while preventing excessive stress on the bellows assembly. During tests, it was typical to observe slow drifting of the backpressure level, with variations during individual tests considered negligible.

Measurement Instrumentation

Instrumentation included pressure transducers, temperature sensors, power input measurement, flow measurement, and Dewar liquid-level measurement devices as discussed in the following sections.

Pressure

Pressures were measured at a tap in the top plate of the bellows and at a static tap inserted in the flow path downstream of the test section. The taps were connected with copper tubing to direct-reading pressure gauges. The precision of the transducers was reported to be ±7 Pa. The pressure measurement at the bellows P_1 was not reliable because of the unknown liquid level in the tubing connecting the tap and transducer. Therefore, the use of P_1 was restricted to sensing the onset of liquid outflow from the bellows. The downstream measurement P_2 was a good measure of system pressure in the near-horizontal section of the apparatus.

Temperature

Silicon diode temperature sensors were used to measure preheater inlet, test section inlet, and test section wall temperatures (at six locations). Each diode was individually calibrated by the manufacturer to an accuracy of ±50 mK.

A thermocouple made from Chromel-constantan wire was used to measure the radiation shield cooling flow at the entrance to the heat exchanger. The reference junction was a simple ice bath. This temperature measurement did not require high accuracy but was simply used to monitor the shield temperature. Output voltages from thermocouple reference tables were used to construct a polynomial curve-fit equation to obtain temperatures.

Power Input

Electrical power inputs to the preheater and test section were supplied by dc power supplies located in the control room. Precision resistors of 1.16 and 10 Ω were connected in series with the preheater and test section, respectively. Voltage drops across these resistors were measured and used to compute current levels:

$$i_{ph} = \frac{V_{RA}}{1.16} \qquad (2)$$

$$i_{ts} = \frac{V_{RB}}{10} \qquad (3)$$

where i_{ph} and i_{ts} are the electrical current of the preheater and the test section, respectively, and V is the voltage. The currents and the measured voltage drops across the preheater and test section were then used to calculate the power (heat) inputs $\dot{Q}_{ph}$ and $\dot{Q}_{ts}$:

$$\dot{Q}_{ph} = i_{ph}V_{ph} \qquad (4)$$

$$\dot{Q}_{ts} = i_{ts}V_{ts} \qquad (5)$$

Flow Metering

The calibrated bellows was the flow-metering device. Daney (ref. 4) calibrated the bellows using a bell-type gas prover and determined a linear displacement rate of 247 cm^3 per revolution of the drive screw. The calibration includes compensation for thermal contraction to cryogenic temperatures. Three pull rods equally spaced around the bellows prevent lateral deflections. Reported values of volumetric flow rate are observed at the bellows exit. Mass-flow-rate calculations are based on density calculations using the downstream pressure and preheater inlet temperature and assume steady-state conditions with no mass storage or removal in the flow path.

Liquid Level

The supply Dewar was equipped with a capacitance probe to determine liquid level. This device, calibrated for liquid hydrogen, was utilized only during filling of an initially empty Dewar. A point sensor positioned at the maximum liquid-level position was used as an indicator during filling and topoff. During testing, the Dewar was generally topped off between runs.

Vacuum

The vacuum level in the vacuum jacket was measured by an ionization gauge on the portable air-cooled diffusion pump system. The pump gauge had an autoranging feature and spanned vacuum pressures from 100 to 10^{-6} Pa.

Data Processing

Data Acquisition

Qualitative video data of the two-phase flow patterns were recorded on videotape in super-VHS format by a color digital video camera viewing the downstream port. The CCD-type camera had an effective resolution of 330 000 pixels, was equipped with an automatic iris for exposure control, and had a closeup lens for magnification. A time-date generator stamped the video with the time and date. It was necessary to add or remove additional light shielding to compensate for sunny or cloudy conditions. The video system was monitored from within a control room and greatly aided in the operation of the apparatus. The time stamp on the video allowed synchronization with temperature and pressure data from computer files.

A microcomputer that was used for quantitative data acquisition had an IEEE 488 interface board which communicated with a data-acquisition control unit. The control unit sampled data from the pressure transducers, silicon diodes, and thermocouple. Voltage drops across the preheater, test section, and the two precision resistors for measuring current levels

were sampled by the control unit. It also provided the 10-μA input current for the silicon diode temperature sensors. The software that controlled the system was written in BASIC and used the individual calibration equations to convert the silicon diode outputs to temperature. Similarly, the polynomial curve fit for the thermocouple was programmed into the data-acquisition software. Data were sampled at 5- or 30-s intervals and could be displayed in either text or graphical (temperatures only) format. When desired, the data were stored on the computer hard disk.

Initially, the data-acquisition control unit was connected to the stepper motor controller via an RS–232 connection. It was quickly observed that the stepper motor produced electric noise that interfered with the temperature measurements, so the RS–232 connection was disconnected and the motor was controlled manually.

In general, the high-impedance, silicon diode sensors were sensitive to interference from electrical noise, so several noise-reduction techniques were applied. The current and voltage leads for the silicon diodes were made from coaxial cable and grounded to the data-acquisition control unit. The stepper motor controller, a major source of noise, was placed on a separate electrical power circuit and was connected to it through a power-conditioning and filtering device.

Video Data Reduction

By carefully reviewing the videotapes, with frequent use of slow-speed playback, each test point was classified by flow pattern. Flow pattern identification and classification are subjective processes; therefore, some initial classifications were revisited and were sometimes revised as additional data and experience were accumulated. It should be noted that the apparatus did not allow a global view of the flow, sometimes making it difficult to deduce the overall behavior of the flow being observed. Following the lead of Taitel (ref. 5), the observed flow patterns were grouped into four major categories. A qualitative description of each category follows.

Annular.—Generally the entire wall remains wetted and liquid is seen streaming along the wall. The thickness of the film at the bottom can be substantially greater than it is at the top. The interface appears somewhat opaque because of interfacial turbulence, as one cannot readily see through the tube.

Near transition, as the gas superficial velocity u_G^s is reduced, the upper wall is close to dryout and may dry out on an intermittent basis.

At a high u_G^s, the flow is very fast and very turbulent. The interface becomes more opaque and the lower film thickness is greatly reduced but is still thicker than at the top. The entire wall is clearly wetted at all times.

Bubble.—Bubble flow was not observed in the present work, but at the lowest u_G^s and higher liquid superficial velocity u_L^s combinations, there are a few cases where the bubbles are nearly spherical or are at least short compared with the window length. It is speculated that these conditions indicate a proximity to pure bubble flow that could exist if u_L^s were increased beyond the range of data.

Intermittent.—At the lowest u_G^s, a laminarlike flow of bubbles passes through the window. This is called plug flow. The bubbles are in the uppermost part of the tube, occupying from one-third to two-thirds of the tube diameter and may be much longer than the tube diameter. The bubbles can be short, less than or about equal to the window length. In a few cases, the bubbles are shorter yet and seem to be the result of coalescence of a small number of spherical bubbles. The interface is generally glasslike.

At higher u_G^s, the flow pattern is more rapid and turbulent-like, and the interface is not smooth. This is slug flow. The liquid between gas slugs is similar in shape to wave crests and generally moves by too fast for details to be observed. It was not possible to determine if the slugs were aerated (if they contained entrained bubbles).

The transition between the plug and slug subregions is gradual and much of the intermittent data seem to be a combination of the two patterns.

Stratified.—According to Taitel (ref. 5), this flow is not observed for upward-inclined flow except at very shallow angles of inclination. It does not seem to appear in the present data, with the exception of two situations: when dryout is occurring and during transition from annular to intermittent flow.

A cyclical type of flow occurs when the stratified liquid level slowly decreases due to evaporation and eventually disappears altogether. After a short interval of completely dry conditions, a new liquid layer comes into view and the process is repeated. This is classified as stratified-dryout flow.

There is another transition-region flow pattern in which the flow is neither intermittent nor annular. It appears as a stratified flow with intermittent wispy bursts passing through the gas layer. These wispy bursts are similar to those seen in annular flow, or perhaps mist flow, which was not otherwise observed. This flow is classified as wavy-annular flow and will be discussed in more detail in the section Nitrogen Results.

Quantitative Data Reduction

The two-phase flow parameters are computed from the thermodynamic equilibrium quality x, where the quality is calculated from an energy balance using the volumetric flow rate $\mathscr{V}$, inlet temperature T_{in}, system pressure P_{ts}, preheater power input $\dot{Q}_{ph}$, heat leak $\dot{Q}_{lk}$, and total test section power input $\dot{Q}_{ts}$. (Total test section power input is used because the flow pattern was videotaped at the downstream viewport.) All these quantities were measurable except heat leak, which was experimentally determined. Heat leak is discussed in the next section.

$$x = \frac{h_{tp} - h_f}{h_g - h_f} \tag{6}$$

where

$$h_{tp} = h_{in} + \frac{\dot{Q}_{tot}}{\dot{m}} \qquad (7)$$

$$\dot{Q}_{tot} = \dot{Q}_{ph} + \dot{Q}_{lk} + \dot{Q}_{ts} \qquad (8)$$

$$h_{in} = h_{in}(T_{in}, P_2) \qquad (9)$$

$$h_f = h_f(P_2) \qquad (10)$$

$$h_g = h_g(P_2) \qquad (11)$$

and

$$\dot{m} = \rho_{in}(T_{in}, P_2)\dot{\mathcal{V}} \qquad (12)$$

where h is the specific enthalpy, P_2 is the downstream pressure, $\dot{m}$ is the mass flow rate, ρ is the density, and the subscripts tp, f, g, in, and tot denote two-phase fluid, saturated liquid, saturated vapor, inlet, and total conditions.

Knowing the equilibrium quality and mass flow rate, the superficial velocities can be calculated as

$$u_G^s = \frac{\dot{m}}{A} \frac{x}{\rho_g} \qquad (13)$$

and

$$u_L^s = \frac{\dot{m}}{A} \frac{(1-x)}{\rho_f} \qquad (14)$$

where A is the cross-sectional area of the flow path.

In two-phase flow with heat input, it is generally incorrect to assume thermal equilibrium of the phases. In the present apparatus, the preheater was carefully designed to avoid superheating of the vapor. Inspection of the data revealed few departures from the saturation temperature at the test section inlet or test section based on the measured system pressure. Indications are that the equilibrium assumption is generally valid for the present experiment. Special circumstances where the equilibrium assumption was violated are identified in the discussion of results.

Heat Leak

Test Conditions and Data Analysis

Heat leak tests were conducted to determine the steady-state environmental heating rate for the apparatus. Three tests were conducted using liquid nitrogen (LN_2) and one with liquid hydrogen (LH_2). Since the two-phase quality and void fraction within the apparatus could not be determined, it was necessary to perform the heat leak tests with single-phase fluid (liquid) in the system. The apparatus was operated at stepper motor speeds ranging from 0.0001 to 0.001 rps without power input to the preheater or test section. After approximately 30 to 60 min of operation, initial transients subsided and the rates of change of preheater inlet, test section inlet, and test section temperatures became constant. Data from this quasi-steady condition were sampled for approximately 10 min. Much of the liquid within the apparatus became superheated as a result of the very low flow rates and long time span of the pretest transients. The length of the tests during quasi-steady conditions was limited by the eventual transition to two-phase conditions at the onset of boiling. The heat leak was determined for the portion of the apparatus from the preheater inlet to the test section. In the flow pattern tests, the preheater inlet condition is treated as a single-phase (liquid) reference point at a known temperature and pressure. Thus, the heat leak correction is directly applicable to calculations starting with the preheater inlet reference point.

The control volume for the heat leak analysis is the flow channel from the preheater inlet to the downstream end of the test section. Heat leak into the control volume is a transient process characterized by heating of the tube wall, the liquid within the control volume, and the liquid exiting the control volume. An unsteady-state energy balance following standard thermodynamic fundamentals (ref. 6) was applied to the control volume as follows. The control volume was divided into four unequal volumes according to the locations of temperature measurement points. A FORTRAN program was written to numerically evaluate the following equations at each node of the control volume using fluid properties from GASPAK (ref. 7). Time-dependent temperatures and system pressure were obtained from linear curve fits of the data. The data show a gradual rise in mean temperature at each measurement location along with some scatter attributed to unsteadiness due to uneven heating and electrical noise.

The heat leak is calculated as

$$\dot{Q}_{lk} = \frac{\Delta \mathcal{U}_L + \Delta \mathcal{U}_w + H_{out} - H_{in}}{\Delta t} \qquad (15)$$

where $\mathcal{U}_L$ and $\mathcal{U}_w$ are the total internal energy of the liquid and the wall, H_{out} and H_{in} are the total enthalpy flow at the outlet and the inlet, t is the time, and

$$\Delta \mathcal{U}_L = \sum_{j=1}^{4} \left[(\rho_L \mathcal{V}_L \mathcal{u}_L)_{final,j} - (\rho_L \mathcal{V}_L \mathcal{u}_L)_{init,j} \right] \qquad (16)$$

where $\mathcal{V}_L$ is the volume of the liquid, $\mathcal{u}_L$ is the specific internal energy of the liquid, and

$$H_{out} - H_{in} = \int_{t_{init}}^{t_{final}} \dot{m}_{out} h_{out} \, dt - \int_{t_{init}}^{t_{final}} \dot{m}_{in} h_{in} \, dt \qquad (17)$$

and

$$\Delta \boldsymbol{u}_w = \sum_{j=1}^{4} \sum_{k=1}^{8} m_{w_{j,k}} c_{p_{j,k}} \left(T_{w_{j,\text{final}}} - T_{w_{j,\text{init}}} \right) \qquad (18)$$

where m is the mass, the j summation index represents the volume or wall segment, and the k index represents the wall material.

Superheated liquid properties were computed using the following relations:

$$\rho_L = \rho_f + \left. \frac{\partial \rho_f}{\partial P} \right|_{\text{sat}} \left(P_2 - P_{\text{sat}} \right) \qquad (19)$$

$$h_L = h_f + c_{p,\text{sat}} \left(T - T_{\text{sat}} \right) \qquad (20)$$

$$\boldsymbol{u}_L = h_L - \frac{P_2}{\rho_L} \qquad (21)$$

Heat Leak Test Results

In the LN_2 tests, the heat capacity of the flow channel wall absorbs approximately 10 percent of the heat input. This quantity is negligible in the LH_2 test. Calculation of the wall energy change at each node is based on the measured temperature change and the specific heats and estimated mass of each material used in that node.

The steady-state heat leak from the preheater inlet to the downstream end of the test section was calculated to be 0.22 ± 0.17 W (2-sigma confidence level). This value is used in the flow pattern analysis for the calculation of the thermodynamic equilibrium quality x. More details are provided in table I. Although the uncertainty is large on a relative basis, its magnitude is small and has little impact on the analysis of the flow pattern data unless the two-phase quality is very near zero.

A look at temperature gradients along the flow path indicated that axial wall conduction was not significant at either end of the control volume for the heat leak analysis. Under steady-state, two-phase flow conditions, the heat leak can be expected to remain nearly the same with the total heat leak entering the flow stream.

Flow Pattern Transition Models

Overview

The analytical prediction of the flow pattern maps for this work is based on Taitel's (ref. 5) "unified model," which incorporates a large number of earlier results (refs. 8 to 10). A thorough reading of Taitel's paper and supporting references is necessary for complete understanding of the predictive tools. The unified model is applicable to any angle of flow inclination β and pipe diameter D. Various properties of the liquid and gas phases are required inputs. The boundary between two flow patterns on a flow pattern map is determined by developing a transition mechanism based on physical concepts. By obtaining a mathematical balance of the physical transition model, the corresponding flow pattern boundary can be obtained.

As reported by Barnea, Luninski, and Taitel (ref. 11), flow patterns in horizontal flow are affected by capillary forces in small-diameter tubes at low liquid and gas flow rates. For horizontal air-water flow, they report a modified stratified-smooth to intermittent flow transition for pipe diameters of 6 mm or less, whereas diameters of 8.15 mm or greater did not exhibit surface tension effects. A pipe Bond number Bo can be defined to characterize the relative importance of surface tension and gravitational forces:

$$Bo = \frac{(\rho_L - \rho_G)gD^2 \cos\beta}{\sigma} \qquad (22)$$

where g is the acceleration due to gravity and σ is the surface tension.

Our calculations based on the air-water results of Barnea, Luninski, and Taitel show that surface tension effects occur for Bo less than 5 but not for Bo greater than 9. The Bond numbers for our nitrogen and hydrogen data are 66 and 27, respectively, so we need not consider the modified transition for small-diameter pipes and will use the standard predictive models.

There is a general requirement in the models to specify friction factors based on laminar or turbulent flow conditions. The transition criterion is modeled after single-phase flow in a pipe with the laminar-to-turbulent transition occurring at Reynolds numbers from 2100 to 4000 (ref. 12). Some overlap

TABLE I.—HEAT LEAK TEST RESULTS: PREHEATER INLET TO DOWNSTREAM END OF TEST SECTION

Test number	Test fluid	Duration, min	Motor speed, rps	Rate of heat leak, $\dot{Q}_{lk}$, W	Liquid heating fraction, $\Delta \boldsymbol{u}_L / \dot{Q}_{lk}$	Wall heating fraction, $\Delta \boldsymbol{u}_w / \dot{Q}_{lk}$	Net enthalpy flow fraction, $\Delta H / \dot{Q}_{lk}$
g12	Liquid hydrogen	12.0	0.0010	0.283	0.09	0.00	0.91
d80	Liquid nitrogen	11.5	.0001	.110	.43	.14	.43
e32	Liquid nitrogen	14.5	.0005	.291	.13	.04	.83
e50	Liquid nitrogen	8.8	.0001	.199	.36	.10	.53

is necessary for convergence of computed predictions in the transition region and thus no attempt was made to fine-tune results falling in the transition region.

The following discussion documents the analytical foundations of the computer codes developed to predict flow pattern maps. The three pertinent transition models for this work are (1) existence of bubble flow, (2) transition from stratified flow, and (3) transition from annular flow. Each of the primary transition models will be presented in a manner that can be readily extended to computer coding. Various typographical errors in the original sources have been corrected. In each case, a transition curve is plotted on a two-dimensional map having the gas and liquid superficial velocities as coordinates for comparison with experimental data.

Existence of Bubble Flow

Bubble flow is divided into two subcategories—bubbly and dispersed bubble. Bubbly flow occurs only in vertical and off-vertical pipes and therefore is not pertinent to the current experiment. Dispersed bubbles tend to exist at high liquid flow rates with the bubble dispersion caused by turbulence. Barnea, Shoham, and Taitel (ref. 10) calculate the dispersed bubble diameter d_C as

$$d_C = \left(0.725 + 4.15\sqrt{\alpha}\right)\left(\frac{\sigma}{\rho_L}\right)^{3/5}\kappa^{-2/5} \qquad (23)$$

where κ is a rate of energy dispersion and

$$\alpha = \frac{u_G^s}{u_m} \qquad (24)$$

$$\kappa = \frac{2}{D}\left[C_m\left(Re_m\right)^{-n_m}\right]u_m^3 \qquad (25)$$

where C is the Blasius friction-factor coefficient, Re is the Reynolds number, n is the Blasius friction-factor exponent, and the subscript m refers to mixture.

The mixture velocity u_m is related to the superficial velocities by

$$u_m = u_L^s + u_G^s \qquad (26)$$

and is used to define the mixture Reynolds number:

$$Re_m = \frac{u_m D}{\nu_L} \qquad (27)$$

where ν_L is the kinematic viscosity of the liquid.

The coefficient and exponent for the Blasius-type friction factor are specified as

$$C_m = \begin{cases} 16, & \text{laminar} \\ 0.046, & \text{turbulent} \end{cases} \qquad (28)$$

and

$$n_m = \begin{cases} 1, & \text{laminar} \\ 0.2, & \text{turbulent} \end{cases} \qquad (29)$$

Dispersed bubbles are approximately spherical and grow in size until one of the following happens:

1. The bubbles coalesce as they deform as a result of their increasing size.

2. The bubbles rise to the high side of the pipe and agglomerate (in horizontal and inclined pipes) in a process known as creaming.

3. The void fraction reaches the maximum packing density for spheres.

The critical diameter for coalescence is

$$d_{CD} = 2\left[\frac{0.4\sigma}{(\rho_L - \rho_G)g}\right]^{1/2} \qquad (30)$$

The critical diameter for creaming is

$$d_{CB} = \frac{3}{8}\frac{\rho_L}{(\rho_L - \rho_G)}\frac{C_m Re_m^{-n_m} u_m^2}{g\cos\beta} \qquad (31)$$

Maximum bubble packing density occurs at $\alpha = 0.52$, which in terms of superficial velocities is

$$u_L^s = \frac{1-\alpha}{\alpha}u_G^s \approx 0.92\, u_G^s \qquad (32)$$

The transition from bubble flow is found by equating the dispersed bubble diameter from equation (23) to the minimum diameter from equations (30) and (31). The computer code specifies u_G^s and searches for a solution to the equality subject to the maximum u_L^s constraint of equation (32). If a root does not exist, the solution is given by equation (32). The transition curve is produced by performing the process over a range of u_G^s. Dispersed bubble flow occurs for u_L^s greater than the transition value.

Transition from Stratified Flow

It is assumed that stratified flow with the denser liquid flowing on the bottom prevails unless surface waves become

unstable and transition to annular or intermittent flow occurs. The transition is assumed to be a form of the classical Kelvin-Helmholtz instability modified for inclined flow in a pipe. A force balance by Taitel and Dukler (ref. 8) applied to a liquid wave in stratified flow in an inclined pipe results in

$$F^2 \left(\frac{\tilde{u}_G^2}{\mathcal{C}_2^2} \frac{\mathrm{d}\tilde{A}_L}{\mathrm{d}\tilde{\hbar}_L} \frac{1}{\tilde{A}_G} \right) = 1 \tag{33}$$

where F is a modified Froude number

$$F = \sqrt{\frac{\rho_G}{(\rho_L - \rho_G)}} \frac{u_G^s}{\sqrt{Dg \cos\beta}} \tag{34}$$

and $\mathcal{C}_2$ is the coefficient from wave stability criteria, $\tilde{A}_L$ is the dimensionless cross-sectional flow area of the liquid, and the dimensionless liquid level $\tilde{\hbar}_L$ is

$$\tilde{\hbar}_L = \frac{\hbar_L}{D} \tag{35}$$

and $\mathrm{d}\tilde{A}_L / \mathrm{d}\tilde{\hbar}_L$, $\mathcal{C}_2, \tilde{A}_G$, and $\tilde{u}_G$ are functions of $\tilde{\hbar}_L$:

$$\frac{\mathrm{d}\tilde{A}_L}{\mathrm{d}\tilde{\hbar}_L} = \sqrt{1 - \left(2\tilde{\hbar}_L - 1\right)^2} \tag{36}$$

$$\mathcal{C}_2 = 1 - \tilde{\hbar}_L \tag{37}$$

$$\tilde{A}_G = 0.25\left[\cos^{-1}\left(2\tilde{\hbar}_L - 1\right) - \left(2\tilde{\hbar}_L - 1\right)\sqrt{1 - \left(2\tilde{\hbar}_L - 1\right)^2} \right] \tag{38}$$

$$\tilde{u}_G = \frac{\tilde{A}}{\tilde{A}_G} \tag{39}$$

For fixed u_G^s, ρ_G, ρ_L, g, β, and D, the left-hand side of equation (33) is a monotonic function of the liquid level $\tilde{\hbar}_L$. For a specified u_G^s, equations (33) through (39) are solved by numerical iteration to find $\tilde{\hbar}_L$ at the transition from stratified flow. The transition curve is obtained by generating u_L^s for each specified u_G^s. Now the dimensionless hydraulic diameter of the gas phase $\tilde{\mathcal{D}}_G$ can be calculated in addition to the gas-side Reynolds number Re_G, which is based on the actual velocity:

$$\tilde{\mathcal{D}}_G = \frac{4\tilde{A}_G}{\tilde{S}_G + \tilde{S}_i} \tag{40}$$

where $\tilde{S}_G$ is the dimensionless wetted perimeter of the gas phase, $\tilde{S}_i$ is the dimensionless liquid-gas interface length, and

$$Re_G = \frac{\tilde{u}_G u_G^s \tilde{\mathcal{D}}_G D}{v_G} \tag{41}$$

where

$$\tilde{S}_G = \cos^{-1}\left(2\tilde{\hbar}_L - 1\right) \tag{42}$$

and

$$\tilde{S}_i = \sqrt{1 - \left(2\tilde{\hbar}_L - 1\right)^2} \tag{43}$$

To this point, the liquid superficial velocity remains unknown. It is obtained from an equation derived by Taitel and Dukler (ref. 8) for a momentum balance applied to the gas and liquid phases of a stratified flow:

$$-X^2 \left(\tilde{u}_L \tilde{\mathcal{D}}_L\right)^{-n_L} \tilde{u}_L^2 \frac{\tilde{S}_L}{\tilde{A}_L} + \left(\tilde{u}_G \tilde{\mathcal{D}}_G\right)^{-n_G}$$

$$\times \tilde{u}_G^2 \left(\frac{\tilde{S}_i}{\tilde{A}_L} + \frac{\tilde{S}_i}{\tilde{A}_G} + \frac{\tilde{S}_G}{\tilde{A}_G} \right) - 4Y = 0 \tag{44}$$

where X^2 is the Martinelli parameter and Y is an inclination parameter. The following liquid-side parameters are functions of $\tilde{\hbar}_L$, as were the gas-side and interfacial parameters:

$$\tilde{A}_L = 0.25\left[\pi - \cos^{-1}\left(2\tilde{\hbar}_L - 1\right) \right.$$

$$\left. + \left(2\tilde{\hbar}_L - 1\right)\sqrt{1 - \left(2\tilde{\hbar}_L - 1\right)^2} \right] \tag{45}$$

$$\tilde{S}_L = \pi - \cos^{-1}\left(2\tilde{\hbar}_L - 1\right) \tag{46}$$

$$\tilde{\mathcal{D}}_L = \frac{4\tilde{A}_L}{\tilde{S}_L} \tag{47}$$

$$\tilde{u}_L = \frac{\tilde{A}}{\tilde{A}_L} \tag{48}$$

The Martinelli parameter and inclination parameter are defined as

$$X^2 = \frac{\left| \left(\dfrac{dP}{dx} \right)_L^s \right|}{\left| \left(\dfrac{dP}{dx} \right)_G^s \right|} \tag{49}$$

$$Y = \frac{(\rho_L - \rho_G) g \sin\beta}{\left| \left(\dfrac{dP}{dx} \right)_G^s \right|} \tag{50}$$

where the liquid- and gas-side pressure gradients are calculated from

$$\left(\frac{dP}{dx} \right)_L^s = \frac{4C_L}{D} \left(\frac{u_L^s D}{\nu_L} \right)^{-n_L} \frac{\rho_L \left(u_L^s \right)^2}{2} \tag{51}$$

$$\left(\frac{dP}{dx} \right)_G^s = \frac{4C_G}{D} \left(\frac{u_G^s D}{\nu_G} \right)^{-n_G} \frac{\rho_G \left(u_G^s \right)^2}{2} \tag{52}$$

(The sign convention for β is positive for upflow, which is the opposite of that used by Taitel and Dukler (ref. 8).) Note that the liquid superficial velocity u_L^s appears in the Martinelli parameter.

Before solving equation (44) (with all necessary substitutions) for u_L^s, the coefficients and exponents for the Blasius-type friction factors must be specified:

$$C_G \text{ and } C_L = \begin{cases} 16, & \text{laminar} \\ 0.046, & \text{turbulent} \end{cases} \tag{53}$$

$$n_G \text{ and } n_L = \begin{cases} 1, & \text{laminar} \\ 0.2, & \text{turbulent} \end{cases} \tag{54}$$

The gas side has a known Reynolds number, so the proper choices for C_G and n_G are set. A critical Reynolds number of 2300 (same as single-phase pipe flow) was used as the point of transition from laminar to turbulent flow. The liquid-side flow condition is not known and is initially assumed to be laminar. Using this assumption, equation (44) is solved for u_L^s. The liquid flow condition may be checked by computing the liquid Reynolds number:

$$Re_L = \frac{\tilde{u}_L u_L^s \tilde{D}_L D}{\nu_L} \tag{55}$$

If Re_L is less than 4000, the solution for a laminar liquid is valid. Otherwise, the values of C_L and n_L are switched to the turbulent case and a new solution for u_L^s is obtained. If the new Re_L is greater than 2100, the turbulent result for u_L^s is considered acceptable. (Because the friction factor expressions have a discontinuity at the critical Reynolds number, it is necessary to have some overlap in the value of critical Reynolds number.) This ambiguity in the critical Reynolds number simply reflects the chaotic nature of the transition process from laminar to turbulent.

Having verified that the choice of the liquid-side flow condition for the friction factor is correct, the liquid superficial velocity has been obtained for the specified gas superficial velocity. The computer program generates the transition boundary curve by repeating the foregoing computations for a sequence of specified superficial gas velocities.

Transition from Annular Flow

Either of two mechanisms can cause a transition from annular flow in the universal flow pattern model:

1. Spontaneous blockage of the gas core as a result of high liquid holdup (low void fraction)

2. Instability of the liquid film as a result of partial liquid downflow (occurs only in upflow)

The first mechanism is assumed to occur when the liquid holdup is half the maximum stable liquid holdup. Expressed in terms of film thickness δ, the transition occurs when

$$\delta^* = \frac{\delta}{D} = 0.064 \tag{56}$$

This is an empirical result that is not based on any rigorous theoretical model and is independent of the inclination angle.

The second mechanism is modeled by balancing the interfacial shear and gravity forces for annular flow in an inclined tube with upflow. A force balance on the gas core and liquid film is used to develop an expression for the interfacial shear stress required to hold up a liquid film of thickness δ:

$$\tau_i = g(\rho_L - \rho_G) D \sin\beta \left(\delta^* - \delta^{*2} \right) \left(1 - 2\delta^* \right)$$
$$+ \frac{1}{32} C_L \rho_L \left(\frac{D}{\nu_L} \right)^{-n_L} \left(u_L^s \right)^{2-n_L} \left[\frac{1 - 2\delta^*}{\left(\delta^* - \delta^{*2} \right)^2} \right] \tag{57}$$

For annular flow, the liquid and gas flows are assumed to be turbulent. These assumptions are checked later when Re_L and Re_G are computed. The coefficients and exponents for the Blasius-type friction factors are the same as those for the stratified transition.

The transition point due to the instability of the film occurs at a condition of minimum shear stress (ref. 5). This point is found by differentiating equation (57) with respect to film thickness and setting the result equal to zero:

$$g(\rho_L - \rho_G)D\sin\beta\left[\left(1-2\delta^*\right)^2 - 2\left(\delta^* - \delta^{*2}\right)\right]$$

$$-\frac{1}{16}C_L\rho_L\left(\frac{D}{\nu_L}\right)^{-n_L}\left(u_L^s\right)^{2-n_L}$$

$$\times\left[\frac{\left(\delta^* - \delta^{*2}\right)+\left(1-2\delta^*\right)^2}{\left(\delta^* - \delta^{*2}\right)^3}\right] = 0 \qquad (58)$$

If a solution to equation (58) exists and lies between zero and the value for spontaneous blockage, this value of film thickness is used to find the transition point. Otherwise, the spontaneous blockage limit controls the transition.

The proper film thickness for the transition is used to compute the void fraction α, velocity u_L, hydraulic diameter $\mathcal{D}_L$, and Reynolds number of the liquid Re_L:

$$\alpha = 1 - 4\delta^* + 4\delta^{*2} \qquad (59)$$

$$u_L = \frac{u_L^s}{1-\alpha} \qquad (60)$$

$$\mathcal{D}_L = 4D\left(\delta^* - \delta^{*2}\right) \qquad (61)$$

$$Re_L = \frac{u_L D_L}{\nu_L} \qquad (62)$$

The liquid-side hydraulic diameter assumes a wetted perimeter equal to the pipe circumference with no contribution from the liquid-gas interface. If Re_L is greater than 2100, the assumption of turbulent liquid is considered valid. If not, it is necessary to repeat the calculations and assume a laminar liquid.

Next, a gas-side expression for the interfacial shear is obtained using a Blasius-type friction factor and an empirical interface friction factor correlation from Wallis (ref. 13):

$$\tau_i = \frac{1}{2}C_G\left(\frac{u_G^s D}{\nu_G}\right)^{-n_G}\left(1+300\delta^*\right)\rho_G\frac{\left(u_G^s\right)^2}{\left(1-2\delta^*\right)^4} \qquad (63)$$

Equation (63) can be rearranged to solve for the remaining unknown, u_G^s:

$$u_G^s = \left[\frac{2\tau_i\left(1-2\delta^*\right)^4\left(\frac{\nu_G}{D}\right)^{n_G}}{C_G\rho_G\left(1+300\delta^*\right)}\right]^{1/(2-n_G)} \qquad (64)$$

At this point, a corresponding u_G^s for the specified u_L^s has been obtained if the assumption of turbulent gas is correct. The gas Reynolds number can be computed by neglecting the liquid film (the assumption used in the derivation of equation (63)):

$$Re_G = \frac{u_G^s D}{\nu_G} \qquad (65)$$

If Re_G is greater than 2100, the turbulent gas assumption is valid. If not, it is necessary to repeat the gas-side calculations assuming a laminar gas.

The computer program generates the annular transition boundary curve by repeating the foregoing computations for a sequence of specified superficial liquid velocities.

Creation of Flow Pattern Map

The procedures in the previous section were programmed in FORTRAN to generate the transition curves. Since there are four major flow pattern categories (annular, bubble, intermittent, and stratified), the transition curves can be used to demarcate the map into four regions corresponding to each flow pattern. The steps followed to create the flow pattern map are

1. Plot the bubble flow transition boundary.
2. Plot the stratified flow transition boundary outside the bubble region.
3. Plot the annular flow transition boundary outside the bubble and stratified regions.
4. Designate the remaining area on the map as the intermittent flow region.

Transition boundary for bubble flow.—The bubble flow transition curve for the baseline case (nitrogen flowing in an 8.74-mm-diameter tube at an upward inclination of 1.5° from horizontal) is shown in figure 5. The mixture flow is turbulent for the entire curve shown. The transition for u_G^s less than 1.3 m/s is controlled by the creaming condition. At higher u_G^s, the transition is due to the maximum bubble-packing constraint. The predicted curve is insensitive to the inclination angle at values near 0° because of the weak $\cos\beta$ dependency in the creaming condition. The transition due to maximum bubble packing remains unchanged by the inclination angle as it depends only on superficial velocities.

Figure 6 shows the effect of tube diameter for nitrogen flow in an 8.74-mm-diameter tube. As shown, the transition due
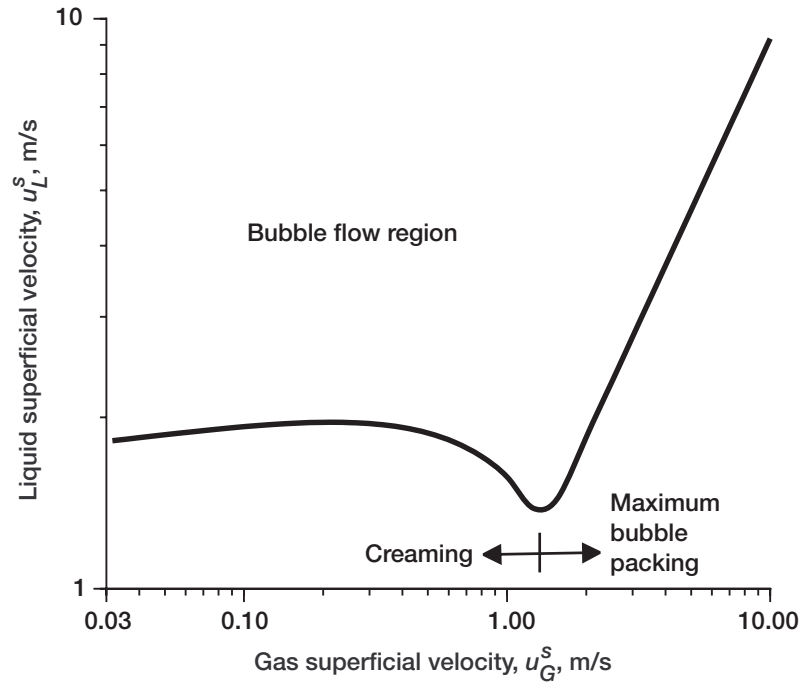
Figure 5.—Predicted transition from bubble flow for nitrogen in 8.74-mm-diameter tube inclined upward at 1.5° from horizontal.
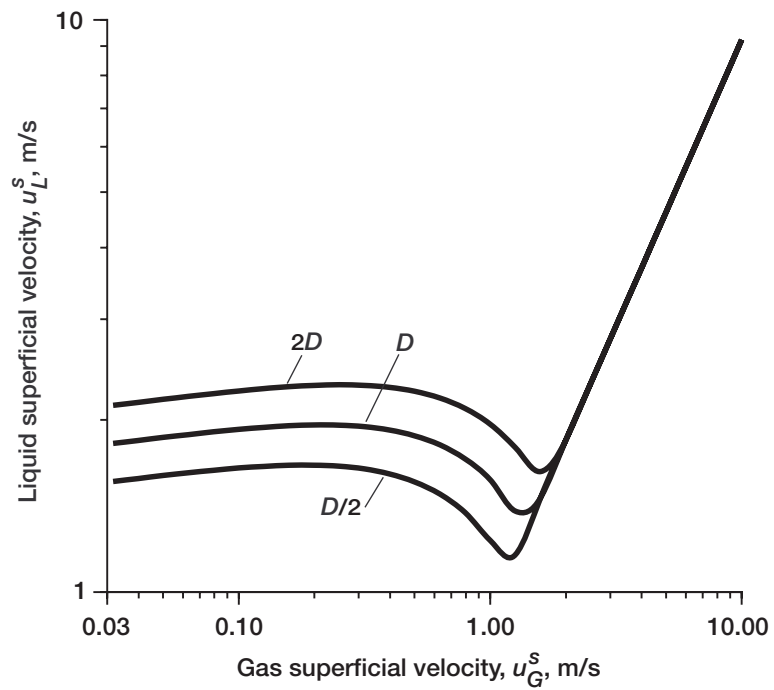

Figure 6.—Effect of tube diameter on predicted transition from bubble flow. Baseline case, nitrogen flow in 8.74-mm-diameter tube inclined upward at 1.5° from horizontal.
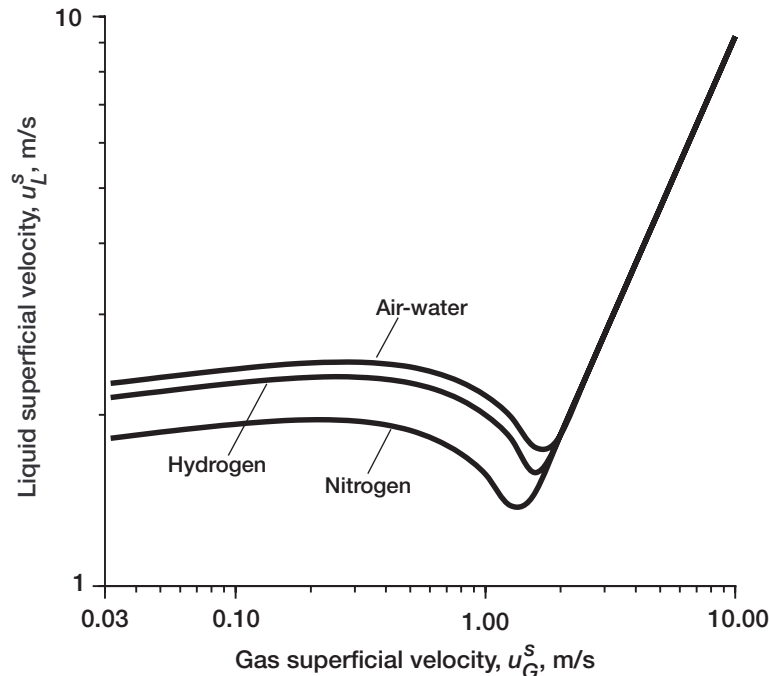
Figure 7.—Predicted transition from bubble flow for nitrogen, hydrogen, and air-water flow in 8.74-mm-diameter tube inclined upward at 1.5° from horizontal. Bubble flow occurs above curves.

to creaming shifts the curve to higher u_L^s as the tube diameter increases. This shift is mainly attributed to the inverse dependence of the bubble energy dispersion on the tube diameter in equation (25). Interestingly, at the larger diameter, the transition at the minimum u_L^s is caused by the coalescence condition.

In figure 7, the bubble flow transition curves for hydrogen and air-water are compared with the nitrogen baseline for an 8.74-mm-diameter tube at 1.5°. The transition curves for hydrogen and air-water are similar. Compared with the nitrogen baseline, there is a shift towards higher u_L^s for the creaming-controlled transition because of differences in fluid properties.

Transition from stratified flow.—This transition is very sensitive to the inclination angle for near-horizontal upflow. Examples are shown in figure 8 for 0°, 0.25°, and 1.5° with nitrogen in an 8.74-mm-diameter tube. As the angle increases, the region for stratified flow rapidly contracts and ultimately disappears at angles of more than a few degrees. The predicted transition for the 1.5° baseline is a slender dome-shaped curve. The gas flow is turbulent and the liquid is laminar for the entire curve shown. For 0.25°, the stratified region expands to higher u_L^s and lower u_G^s. At the top of the dome, the flow is turbulent gas and liquid; otherwise it is turbulent gas and laminar liquid. For horizontal conditions, the transition boundary occurs at an approximately constant u_L^s for low values of u_G^s. This curve has a discontinuity at $u_G^s \approx 0.5$ m/s as a result of the transition from laminar to turbulent flow in the gas-side flow.

Some rather exotic transition curves are predicted for very shallow upward inclination angles. An example for 0.069° with

nitrogen in an 8.74-mm-diameter tube is shown in figure 9. The gap at the discontinuity is substantially greater than that for 0°, and the left curve segment has a sharp bend. The left segment is all laminar gas and liquid flow. The right segment is turbulent gas-turbulent liquid at high u_L^s and turbulent gas and laminar liquid for lower u_L^s. This example is a case in which the laminar-to-turbulent transition modeling has a greater impact and would benefit from further refinement. However, one can question the appropriateness of discriminating between such small differences in inclination for real engineering systems. Another question is, How confidently can the point of laminar-to-turbulent transition be predicted?

The effect of tube diameter on the predicted stratified transition is shown in figure 10 for nitrogen two-phase flow up a 1.5° incline. The main result is a sideways shift with respect to u_G^s: increasing the diameter causes the dome-shaped curve to move to higher u_G^s. In the smaller diameter case, the peak of the curve occurs at a lower u_L^s and the gas is turbulent whereas the liquid remains laminar for the entire curve shown. The larger diameter case is similar to the baseline case with turbulent liquid appearing at the top of the curve. The impact of doubling or halving the diameter is not nearly as significant as making a small change in the inclination angle (on the order of 1° or less) as was discussed in the preceding paragraph.

Predictions for the stratified transition for hydrogen and air-water are compared with nitrogen flow in an 8.74-mm-diameter tube at 1.5° in figure 11. The hydrogen transition curve is similar to the nitrogen curve but shifted to slightly lower u_G^s.
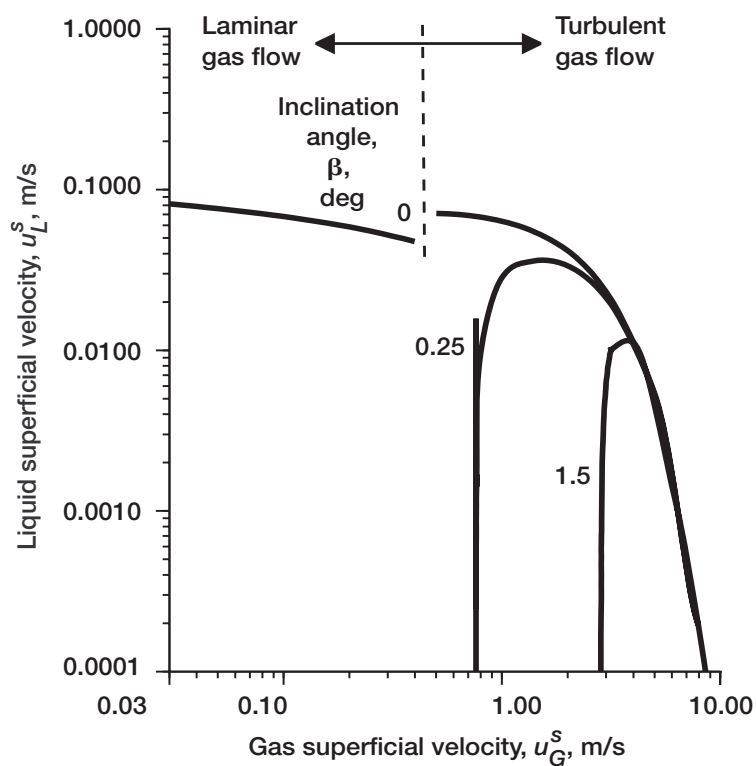
Figure 8.—Effect of tube inclination angle on predicted transition from stratified flow for nitrogen in 8.74-mm-diameter tube. Inclination angle is measured upward from horizontal. Stratified flow occurs below curves.
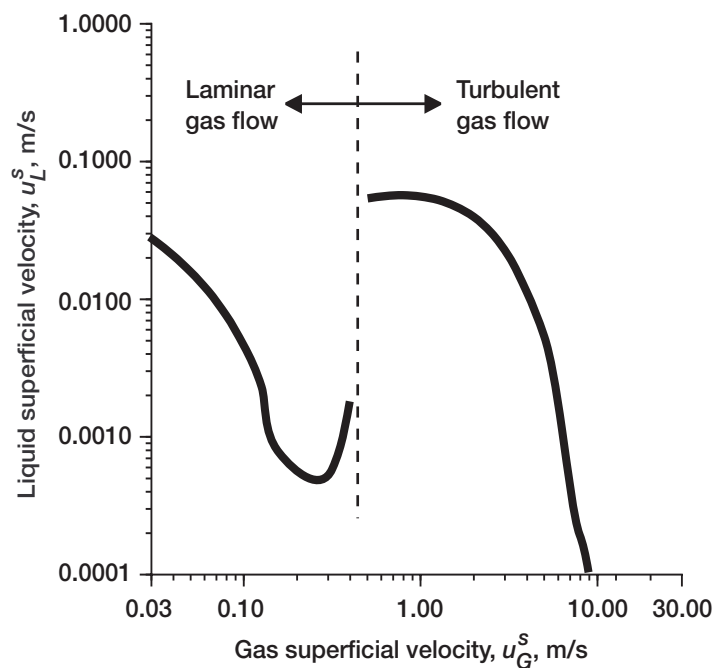

Figure 9.—Predicted transition from stratified flow for nitrogen in 8.74-mm-diameter tube at inclination angle of 0.069° upward from horizontal. Stratified flow occurs below curves.
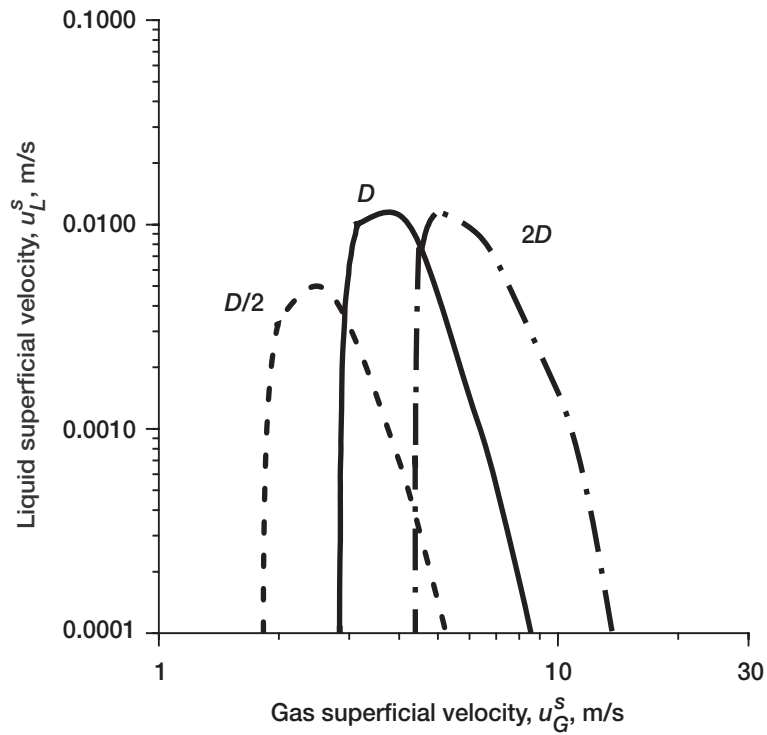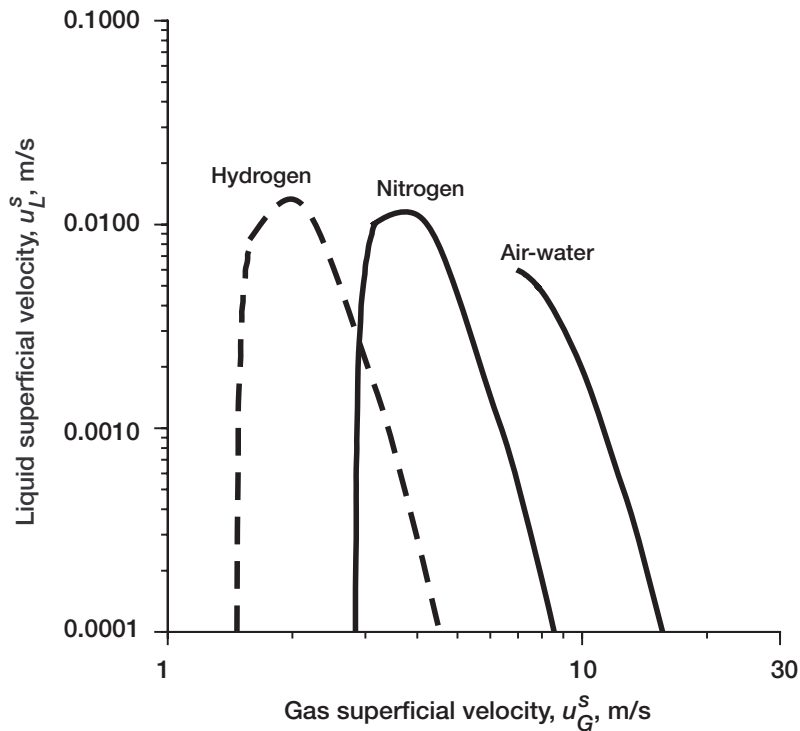
Figure 10.—Effect of tube diameter on predicted transition from stratified flow. Baseline case, nitrogen flow in 8.74-mm-diameter tube inclined upward at 1.5° from horizontal. Stratified flow occurs below transition curves.

Figure 11.—Predicted transition from stratified flow for nitrogen, hydrogen, and air-water flow in 8.74-mm-diameter tube inclined upward at 1.5° from horizontal. Stratified flow occurs below transition curves.

The gas flow is turbulent and the liquid is laminar. The curve for air-water abruptly ends at its u_L^s high point as a result of the discontinuity at the transition to laminar gas conditions. The curve shown is for a turbulent gas-laminar liquid. The behavior of the transition for air-water for these conditions will not be explored further in this work, but it is clearly a topic for more study.

Transition from annular flow.—Predictions for this transition are also sensitive to the inclination angle for near-horizontal flow. The annular transition curves for nitrogen in an 8.74-mm-diameter tube at angles of 0°, 0.25°, 1.5°, and 5° are shown in figure 12. At 0°, the transition mechanism in the region of interest is solely due to spontaneous blockage. The slight offset in the 0° curve at $u_G^s \approx 0.3$ m/s is where laminar-to-turbulent transitions take place in both the vapor and liquid. The remaining curves for the off-horizontal angles show the effect of the film instability transition. The liquid flow is laminar when u_L^s is less than 0.06 m/s and the vapor flow is laminar when u_G^s is less than 0.3 m/s.

The effect of tube diameter is shown in figure 13 for nitrogen flow at β = 1.5°. Increasing the tube diameter shifts the film stability transition towards higher u_G^s but does not affect the transition when controlled by spontaneous blockage because the critical film thickness is proportional to the tube diameter.

Figure 14 shows the predicted transition curves for nitrogen, hydrogen, and air-water in an 8.74-mm-diameter tube at 1.5°. Although the spontaneous blockage limit is specified by a constant value of film thickness or void fraction, the curves for the various fluids are shifted from one another because of differences in fluid properties. One way to think of this is to realize that the interfacial shear force is variable due to the property variations and as a result, the velocity ratios, or slip, are different. The shifts in the transition curves in the stability-controlled region are also apparent for the different fluids.

Predicted Flow Pattern Maps for Nitrogen and Hydrogen

The predictions for the various flow pattern transitions from the previous sections were combined to develop the flow pattern maps for nitrogen and hydrogen flowing in an 8.74-mm-diameter pipe inclined upward at 1.5°. In both cases, the transition curves do not intersect so the process is straightforward. The maps for nitrogen and hydrogen are shown in figures 15 and 16, respectively. The figures are similar, with the hydrogen transitions from annular and stratified flows occurring at slightly lower u_G^s. The experimental results will be compared with these in the section Comparison of Experimental and Predicted Flow Patterns.
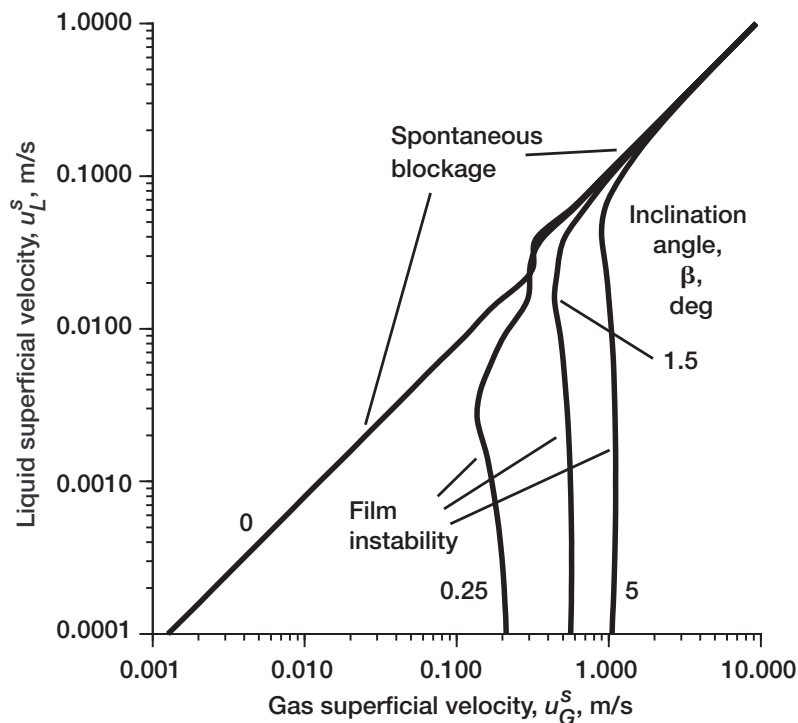

Figure 12.—Effect of tube inclination angle on predicted transition from annular flow for nitrogen in 8.74-mm-diameter tube. Inclination angle measured upward from horizontal. Annular flow occurs to right of curves.
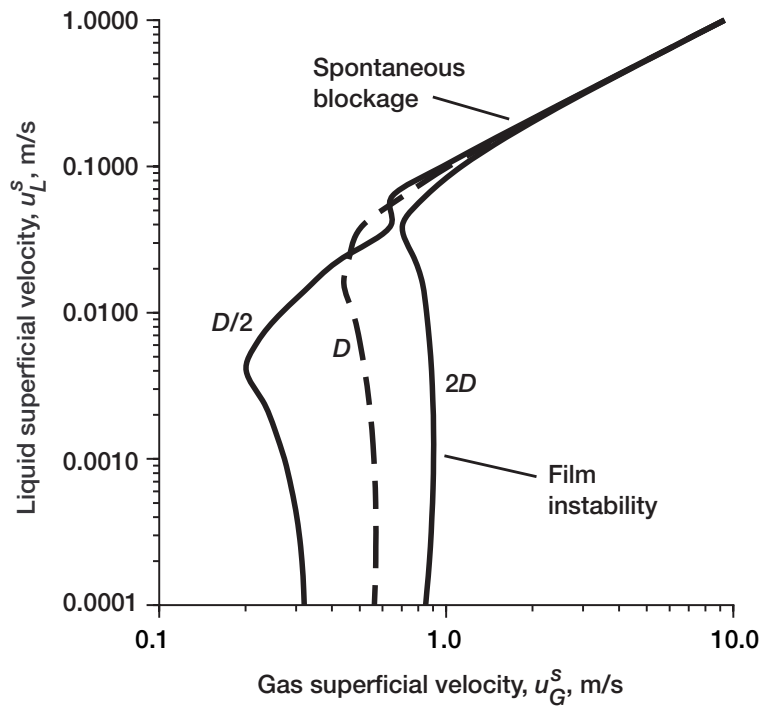
Figure 13.—Effect of tube diameter on predicted transition from annular flow. Baseline case, nitrogen flow in 8.74-mm-diameter tube inclined upward at 1.5° from horizontal. Annular flow occurs to right of transition curves.
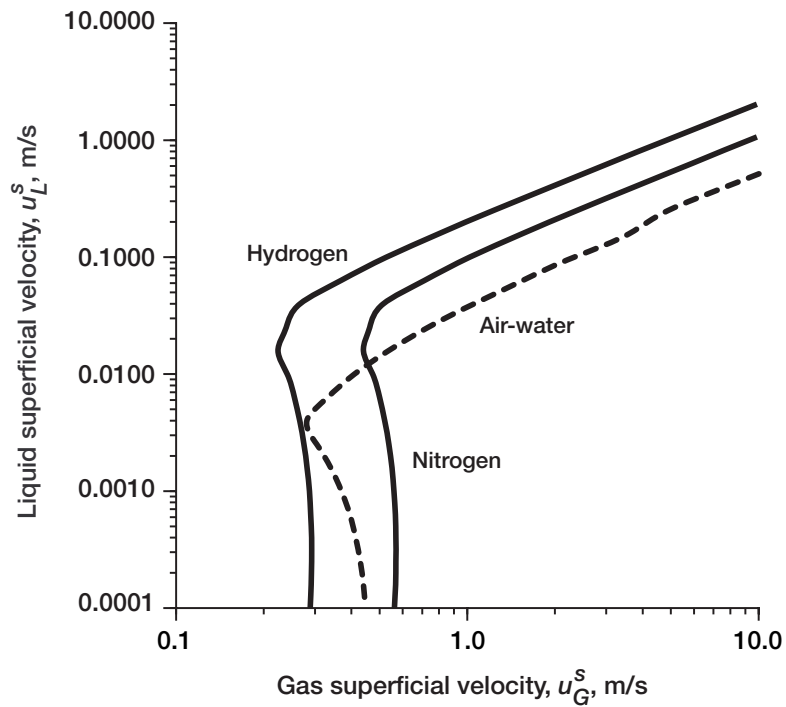

Figure 14.—Predicted transition from annular flow for nitrogen, hydrogen, and air-water flow in 8.74-mm-diameter tube inclined upward at 1.5° from horizontal. Annular flow occurs to right of transition curves.
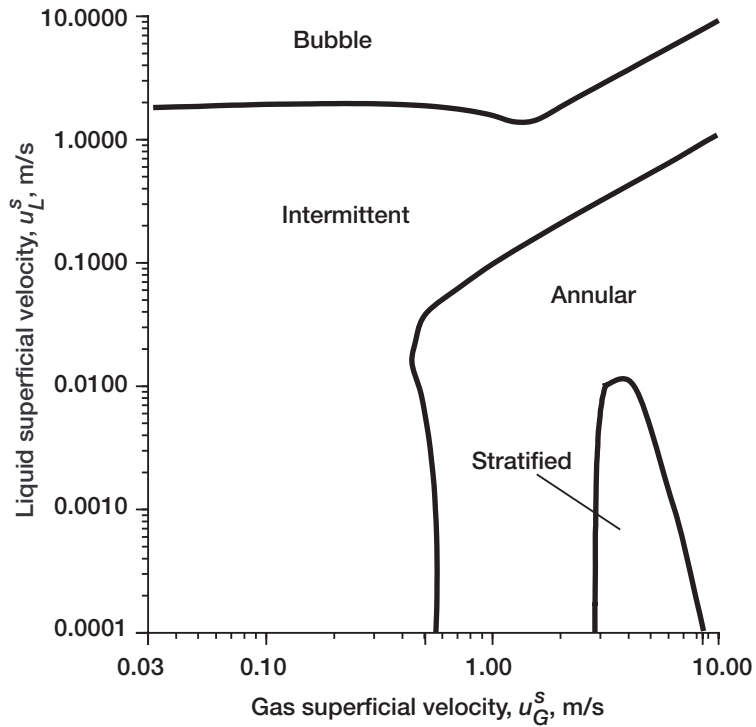
Figure 15.—Predicted flow pattern map for nitrogen in 8.74-mm-
diameter tube inclined upward at 1.5° from horizontal.
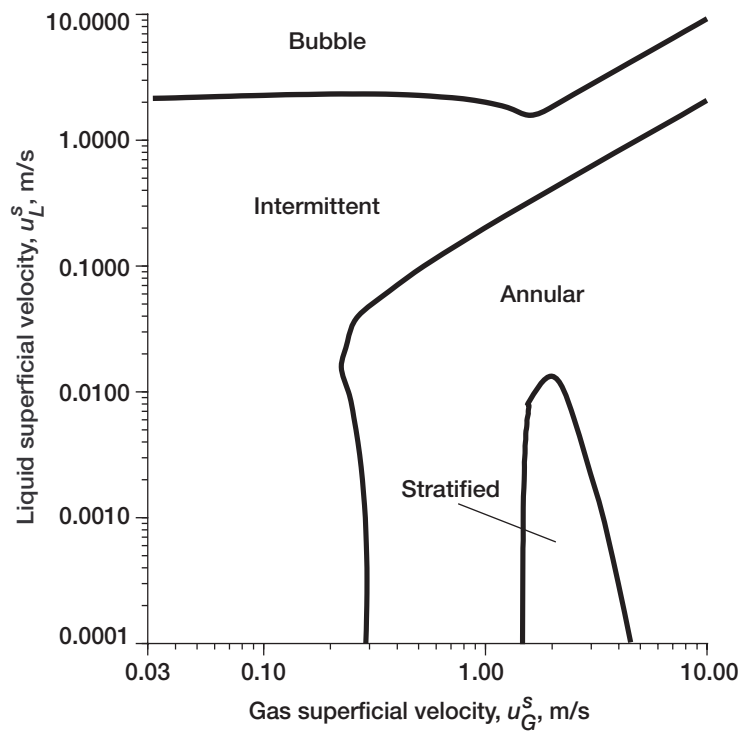
Figure 16.—Predicted flow pattern map for hydrogen in 8.74-mm-
diameter tube inclined upward at 1.5° from horizontal.

Experimental Results

Nitrogen Results

The nitrogen data set contains 102 test points obtained at 5 discrete volumetric flow rates (stepper motor drive speeds of 0.001, 0.003, 0.01, 0.03, and 0.1 rps). Eighty-four plotted points are shown on the experimental flow pattern map for nitrogen in figure 17. The remaining 18 points are duplicates and have been omitted for graphical clarity. When plotted on a conventional flow pattern map with logarithmic superficial velocity coordinates, data for a fixed motor speed lie on a curve that bends downward with increasing heat input. The left side of the curve approaches an asymptote for $x \rightarrow 0$ as $u_G^s \rightarrow 0$ whereas the bottom end of the curve approaches an asymptote for $x \rightarrow 1$ as $u_L^s \rightarrow 0$. The knee of a fixed-flow-rate curve corresponds to $x = 0.5$. The figure indicates that the majority of the data are for x less than 0.5. For the high flow rates, limitations on preheater input power $\left(330 \text{ W max or } \left(u_G^s\right)_{max} \approx 6.5 \text{ m/s}\right)$ prevented us from obtaining data for high equilibrium quality conditions. Another constraining factor is that at high quality, the tube wall dries out and both vapor superheating and the departure from thermal equilibrium start to occur.

Intermittent flow covers the left side of the map. At the lowest u_G^s, the intermittent flow is clearly textbook-quality plug flow: the liquid plugs are substantial and separate the well-defined vapor bubbles under conditions that could be described as laminarlike. As u_G^s is increased, there is a gradual change, with the intermittent flow becoming more agitated (slug flow) and slowly transitioning to other flow patterns. At the far right side of the map, the flow is classic annular flow. The transition from annular flow due to decreasing u_G^s is also a gradual process, and the distinction between intermittent and annular flow is difficult to establish with confidence. We did not see bubbly flow, but think we were approaching bubble flow conditions at the upper left corner of the map where the vapor bubbles were becoming small as compared with the tube diameter.

A special type of stratified flow accompanied by cyclical tube wall dryout was observed as indicated in the lower right region of figure 17. The stratified-dryout flow can be described as a discontinuous flow of liquid along the bottom of the tube. A liquid rivulet appears with oscillating thickness and then slowly thins out, sometimes disappearing due to evaporation. The remaining data points represent a hard-to-categorize flow pattern. It resembles stratified flow except that the gas flow is not completely continuous. Thin, fast-moving wavelike slugs of liquid separate the vapor bubbles and appear somewhat like
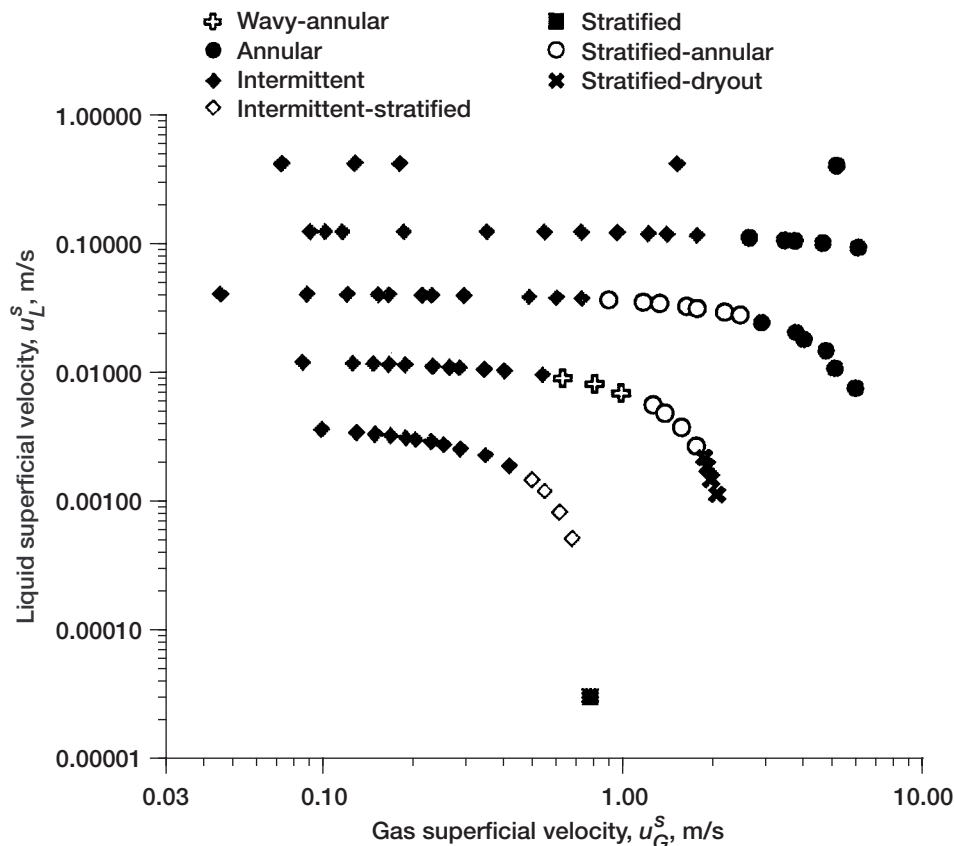

Figure 17.—Experimental flow pattern map for nitrogen in 8.74-mm-diameter tube inclined upward at 1.5° from horizontal.

the wispy bursts associated with annular flow. The frequency of these slugs decreases with increasing u_G^s within the narrow range of occurrence of this flow. We suspect that these points may be near transition to annular flow. As reported by Taitel (ref. 5), the region near intermittent, annular, and stratified flows can be a problematic zone that other researchers have labeled as "proto slug" (ref. 14), "pseudo slug" (ref. 15), and "wavy annular flow" (ref. 8).

Hydrogen Results

We ran fewer hydrogen tests and none at the higher volumetric flow rates because of the limited availability of liquid hydrogen. The data set for hydrogen consists of 46 test points collected at 3 discrete volumetric flow rates (stepper motor drive speeds of 0.001, 0.003, and 0.01 rps). The majority of the data (33 points) are shown in figure 18. Three points corresponding to x greater than 1 are not included but will be discussed shortly. Another 10 points were duplicate points and were omitted for clarity.

Intermittent flow was most frequent whereas bubble and annular flows were not observed. In the upper left corner of the map, a noticeable flow oscillation was seen under intermittent-flow conditions. The vapor bubbles would sometimes undergo either a start and stop motion or a reversal in flow direction.

This oscillatory motion was not observed with nitrogen flow at the 1.5° inclination, but it was observed earlier in the apparatus shakedown testing with nitrogen at 0° inclination. Similar to that seen with nitrogen, stratified flow accompanied by cyclical tube wall dryout was observed in the lower right region of figure 18.

The reader will recall that the quantitative data-reduction procedure assumes that the flow is in thermodynamic equilibrium. During wall dryout, one would question this assumption since the heating of vapor continues beyond the point of dryout. Examination of the test section wall temperatures reveals a cyclical temperature variation that occurred with stratified dryout flow. The temperature excursions above the nominal temperature were minimal near the transition point and then increased in magnitude and duration with further increase in heat input (or decreasing u_L^s as plotted in fig. 18). For the worst case, the excursions were about 8 K and occurred for a total duration of about half the sampling time. Consequently, the positions of the stratified dryout data points as plotted in the figure are not exactly correct, with the error increasing towards the lower right corner. Although these data points should be used with caution, they are considered to be approximately correct. As mentioned earlier in this section, the three additional data points that represent x greater than 1 are not shown. For these points, the computed u_L^s assuming equilibrium are
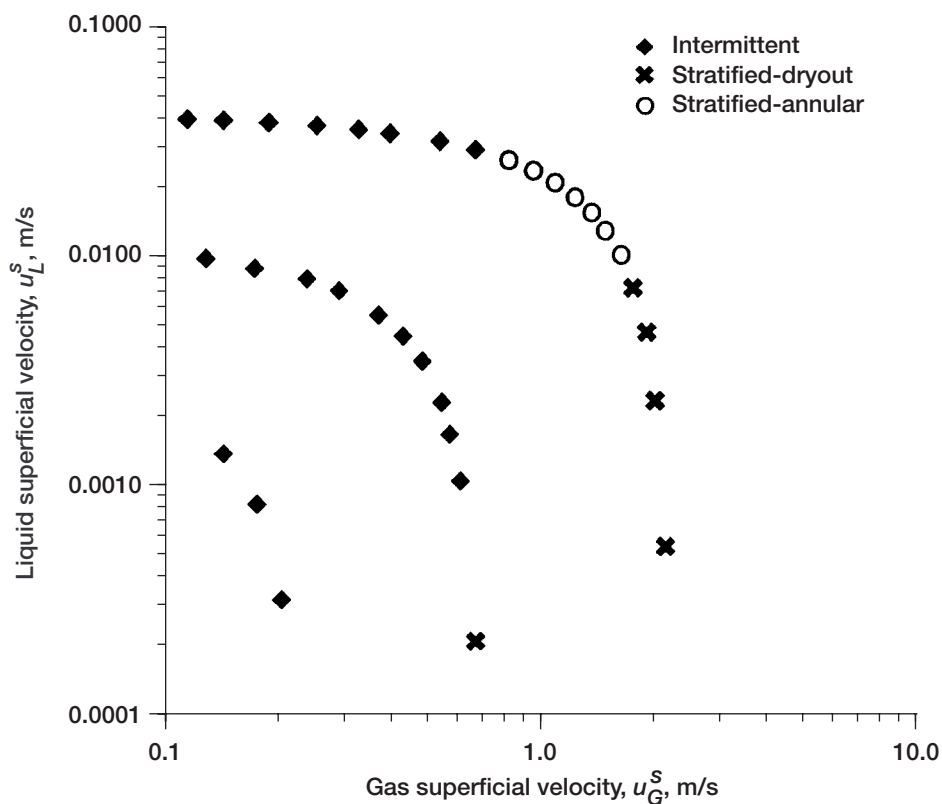

Figure 18.—Experimental flow pattern map for hydrogen in 8.74-mm-diameter tube inclined upward at 1.5° from horizontal.

negative and are obviously incorrect. The flow is unsteady but remains two-phase in a global sense with greater temperature excursions, longer dryout periods, and diminishing liquid flow.

Summary of Experimental Results

Overall, the nitrogen and hydrogen results are similar. We suspect that annular flow could be observed in hydrogen flow by increasing the u_G^s range. Increasing u_L^s may have led to bubble flow for either fluid, but this is more speculative. Intermittent flow is marginally stable under the test conditions, especially with hydrogen. Our ability to determine flow patterns was sometimes limited by the short window length. For example, elongated vapor bubbles in intermittent flow look similar to those in stratified flow except when the liquid plug or slug sandwiched between the bubble ends passes through. The disadvantage of a longer window is that heat leak into the system would be greater.

Comparison of Experimental and Predicted Flow Patterns

The superimposed experimental and predicted flow pattern maps for nitrogen and hydrogen are shown in figures 19

and 20, respectively. The predicted results indicated that we would not observe bubble flow within our range of superficial velocities, as was indeed the case. A complete evaluation of the predicted bubble flow transition will require tests at higher u_L^s than the range of the present data sets. Although the experimental data are not sufficient to validate the bubble flow transition model, the comparison is at least consistent. In the nitrogen map where the u_L^s range extends higher, results at the highest u_L^s fall close to the predicted transition. At these points, the flow pattern was intermittent (plug flow) with the bubble length becoming of the order of the tube diameter. We suspect that these conditions were close to the actual transition to bubble flow but we cannot offer proof.

In essentially all cases where experimental points fell within the predicted intermittent-flow regions, the observed flow was intermittent. For nitrogen, the experimental transition from intermittent flow is in good agreement with the predicted boundary between intermittent and annular flow. The data are consistent with the spontaneous blockage and film instability portions of the annular transition curve (i.e., falling to the left of the transition curve). The hydrogen data are not as extensive and do not include the region near the spontaneous blockage transition; more data will be required to validate this region. For hydrogen, the agreement with the predicted transition due to film instability is not as good: intermittent flow was observed
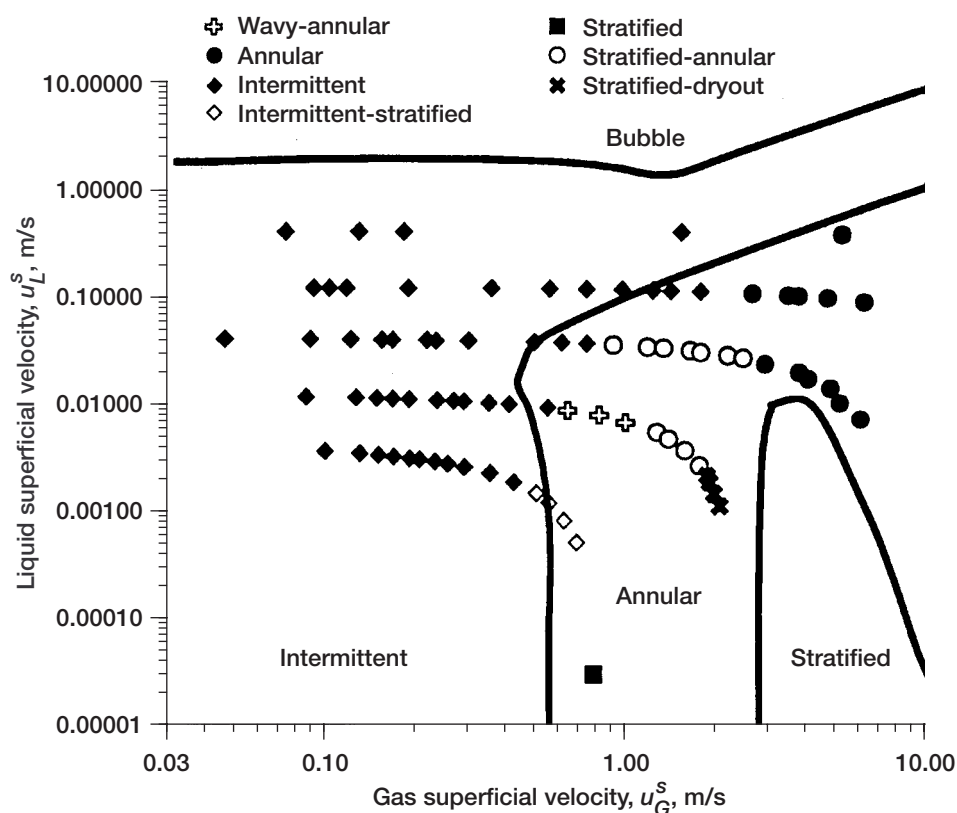

Figure 19.—Comparison of experimental and predicted flow patterns for nitrogen in 8.74-mm-diameter tube inclined upward at 1.5° from horizontal.

at u_G^s values about a half decade higher than the predicted transition boundary. The observations revealed that the transition from intermittent flow to annular and stratified flows is a gradual process without a clear demarcation between them. In view of this, it may not be entirely correct to depict the transition boundary as a thin line but rather as a broad band. An additional comment about the hydrogen data that may or not be pertinent is that some of the hydrogen intermittent flows exhibited instability. The tendency for hydrogen slugs to cyclically reverse flow direction may be a factor that influences the transition to other flow patterns.

For nitrogen, the upper portion of the predicted region of annular flow included all the observed annular flow data points as well as the mixed-flow patterns of stratified-annular and wavy-annular. We consider this to be a reasonably good result. The problematic zone where annular, intermittent, and stratified flows come together is well known. Users of a flow pattern map should be aware of its existence and exercise caution in this region. The agreement is not as good for the hydrogen annular flow comparison. As discussed above, the low u_G^s region of the predicted annular flow zone was observed to be intermittent flow. We did not observe pure annular flow with hydrogen, but we suspect that it would have occurred at higher u_G^s if we could have conducted such tests (this is another region requiring more data). The closest observations of annular flow were what we

call "stratified-annular flow." These data do fall within the predicted annular region of the map as shown in figure 20.

The predictions for stratified flow suggested that this flow pattern would be difficult to observe in the given test apparatus. With nitrogen, we could not operate in this zone and did not generate any data points inside the predicted stratified region. The nitrogen stratified-dryout data fall on the wrong side of the predicted transition but are close considering the sensitivity of the prediction to the inclination angle. We estimate that our reported inclination angle of 1.5° is accurate to within ±0.5° overall. Most likely, the flow path was not perfectly straight and local variations in inclination existed. The high sensitivity of the predicted stratified transition to the inclination angle at small angles makes us wary of the predicted results as well. These factors make us inclined to say that the agreement between experiment and prediction is actually rather good considering the limited amount of stratified flow data. The single stratified flow point for nitrogen is shown for completeness (fig. 19). We did not repeat this test result or obtain similar data in this region as it pertains to nonisothermal conditions that violate the data-reduction assumptions. The majority of the stratified-dryout points fall in the proper position on the hydrogen map. Perhaps it is fortuitous that the predicted stratified region aligns nicely with the highest flow-rate curve for hydrogen and that the prediction appears to be validated by the small number of data
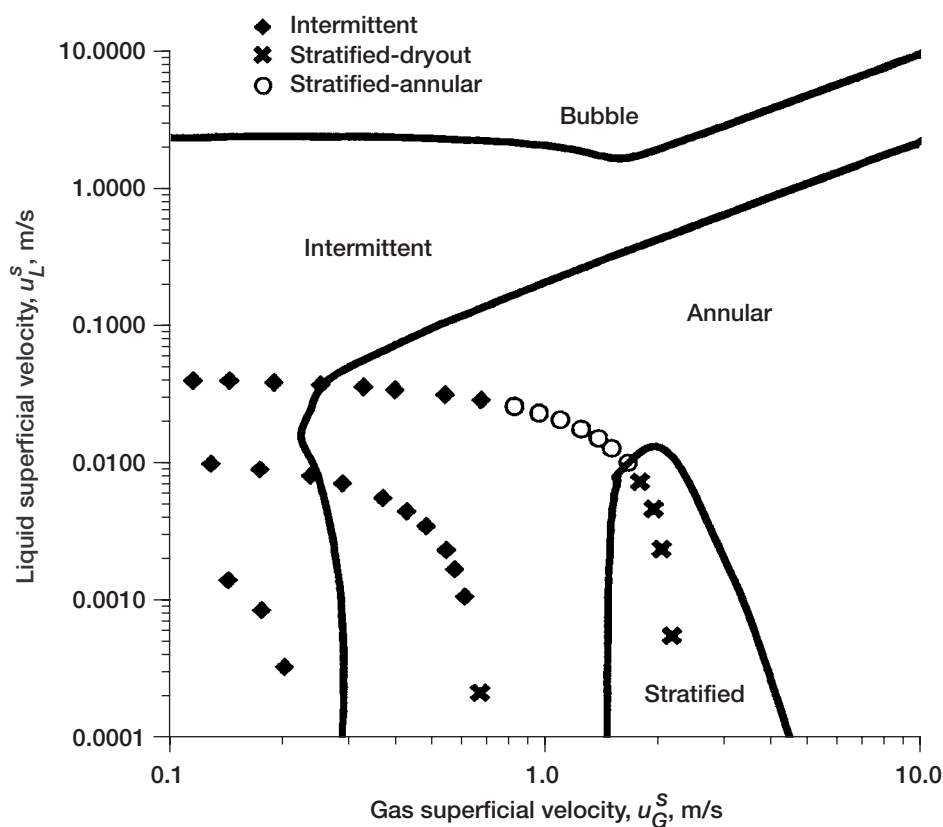

Figure 20.—Comparison of experimental and predicted flow patterns for hydrogen in 8.74-mm-diameter tube inclined upward at 1.5° from horizontal.

points. However, these data are not based on isothermal conditions and the superficial velocities may be somewhat in error.

We are further inclined to suggest that the bottoms of the maps (roughly for $u_L^s < 0.001$ m/s) are subject to the effects of external heat input and phase-change phenomena, neither of which is accounted for in the predictive models. This conjuncture is based on the observation of cyclical tube dryout in this region with both test fluids. The reader is cautioned to use results from this region with care.

Conclusions

An experimental apparatus built and operated at the National Institute of Standards and Technology (NIST) was successfully used to observe cryogenic two-phase flow patterns of nitrogen and hydrogen flowing upward in an 8.74-mm-diameter tube inclined at an angle of 1.5° from horizontal. The data were obtained for steady low mass and heat flux conditions with the majority of the data obtained under conditions of isothermal, saturated flow. Observed flow patterns included intermittent, annular, and stratified but not bubble. The flow pattern results for each fluid are presented in two-dimensional flow pattern maps plotted on superficial velocity coordinates.

At very low liquid superficial velocities ($u_L^s < 0.001$ m/s), the flow was observed to cyclically undergo complete dryout of the tube wall as a result of fluid evaporation due to external heating. Another peculiarity for only hydrogen was an observed instability where the flow exhibited a tendency to cyclically reverse direction if the flow pattern was intermittent and the liquid superficial velocity was high ($u_L^s \approx 0.01$ to 0.1 m/s). This instability could be an apparatus-specific result and was also observed with nitrogen at approximately 0° inclination in the early stages of apparatus checkout.

Computer programs were developed to produce predicted flow pattern maps based on the work of Taitel. The predicted maps were compared with the experimental results and the agreement was favorable considering that Taitel's work has been validated primarily by air-water data and the models do not account for external heating or phase change of the fluid. However, this favorable comparison of cryogenic data with the models is severely limited. Only one angle of inclination and one tube diameter were tested. Bubble flow data are lacking for both fluids and annular flow data are lacking for hydrogen. Nevertheless, the authors think that the models are useful tools which can be used to predict cryogenic flow patterns, provided that these conditions be met:

1. The external heat flux does not exceed 0.1 W/cm^2.
2. The tube diameter is large enough to give a Bond number greater than 10 but is not substantially greater than the present diameter.
3. The inclination angle is near horizontal. If the predicted flow pattern is stratified, additional caution is advised.

Recommendations

Additional work is clearly of value and is recommended as follows:

1. The modeling of the stratified transition at small angles of inclination requires further study. The methods of Taitel are extremely sensitive to small changes in inclination and sometimes exhibit substantial discontinuities in the transition point as a result of transitions from laminar to turbulent flow.
2. External heating and phase change should be incorporated in transition models to allow the prediction of tube wall dryout and its effects on flow patterns. Also, the models could be used with higher levels of heat flux.
3. Experiments at the present inclination angle and tube diameter should be extended to include bubble flow and additional annular flow data.
4. More tests are desired at other inclination angles and tube diameters to allow more extensive validation of the unified flow pattern models.
5. Flow pattern models for space applications should be validated by comparisons with the available two-phase flow data for microgravity. Further work in microgravity is necessary and ideally should include tests with cryogenic fluids.

Glenn Research Center
National Aeronautics and Space Administration
Cleveland, Ohio, September 19, 2001

Appendix—Selected Flow Pattern Samples

A collection of video segments stored on a CD (compact disk) accompanies this report. Each video segment is 1 minute in duration and represents a particular flow pattern observed in the experimental work. The locations of these samples are listed in table II in order of appearance on the disk and are indicated on the flow pattern maps in figures 21 and 22 for nitrogen and hydrogen, respectively.

TABLE II.—VIDEO CLIPS OF FLOW PATTERNS STORED ON COMPACT DISK

| Test number	Fluid	Gas superficial velocity, u_G^s, m/s	Liquid superficial velocity, u_L^s, m/s	Flow pattern
25b	Nitrogen	0.79	0.00003	Stratified
35e		.15	.0033	Intermittent
16d		.70	.00052	Intermittent-stratified
51f		2.0	.0019	Stratified-dryout
60c		.12	.041	Intermittent
26d		0.83	.0080	Wavy-annular
21a		1.8	.031	Stratified-annular
29c		6.1	.0073	Annular
48a		.13	.41	Intermittent
45a		5.3	.38	Annular
21a	Hydrogen	0.14	0.0014	Intermittent
14g		.57	.0017	Intermittent
5f		2.1	.0024	Stratified-dryout
17a		0.14	.039	Intermittent
9d		.54	.031	Intermittent
10b		1.4	.015	Stratified-annular
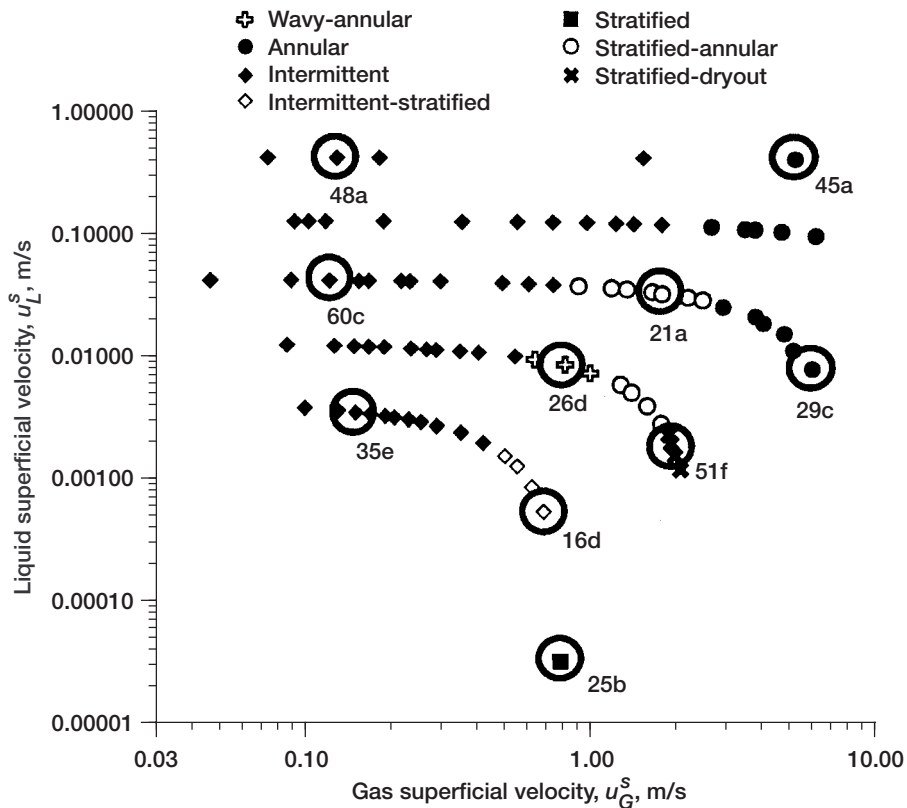
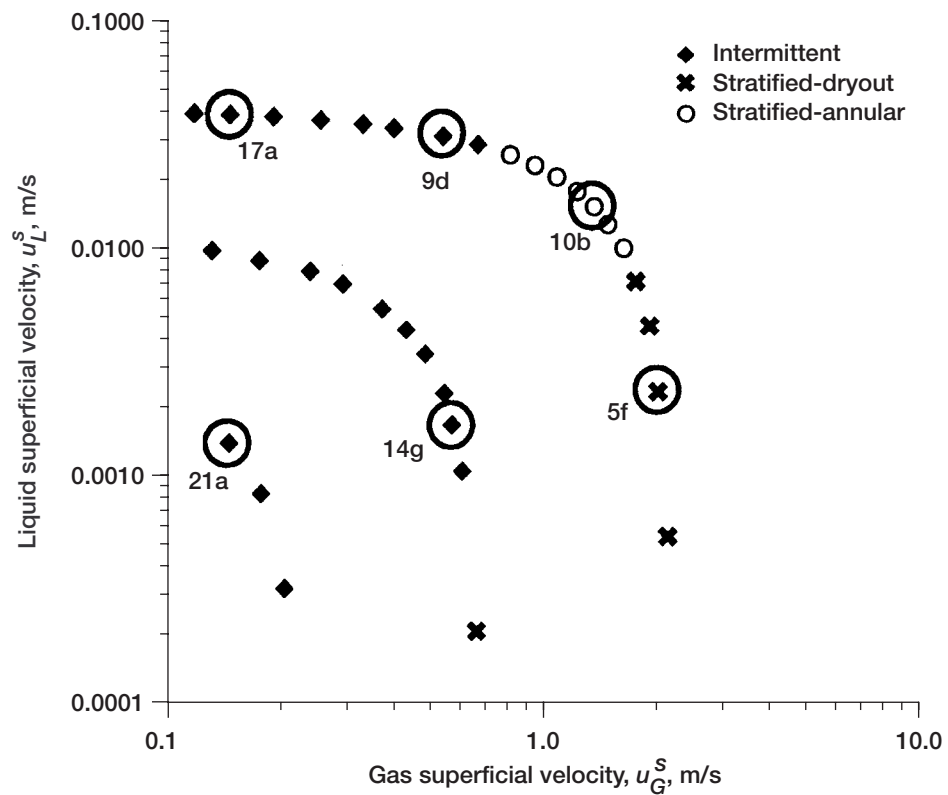Figure 21.—Locations of nitrogen video segments on flow pattern map.

Figure 22.—Locations of hydrogen video segments on the flow pattern map.

References

1. Collier, John G.; and Thome, John R.: Convective Boiling and Condensation. Oxford University Press, Oxford, UK, 1994.

2. Tong, L.S.; and Tang, Y.S.: Boiling Heat Transfer and Two-Phase Flow. John Wiley & Sons, New York, NY, 1965.

3. Baker, Ovid: New Pipeline Techniques: Designing for Simultaneous Flow of Oil and Gas. Oil Gas J., vol. 26, 1954, pp. 185–195.

4. Daney, D.E.: Behavior of Turbine and Venturi Flowmeters in Superfluid Helium. Advances in Cryogenic Engineering, R.W. Fast, ed., vol. 33, 1988, pp. 1071–1079.

5. Taitel, Yehuda: Flow Pattern Transition in Two-Phase Flow. Heat Transfer 1990: Proceedings of the Ninth International Heat Transfer Conference, G. Hetsroni et al., eds., Hemisphere Pub. Corp., New York, NY, 1990, p. 237.

6. Smith, Joseph M.; Abbott, M.; and Van Ness, H.C.: Intro to Chemical Engineering Thermodynamics. McGraw-Hill, New York, NY, 1996.

7. Arp, Vincent; McCarty, Bob; and Fox, Jeff: GASPAK. Computer Program, Cryodata, Inc.

8. Taitel, Yemada; and Dukler, A.E.: A Model for Predicting Flow Regime Transitions in Horizontal and Near Horizontal Gas-Liquid Flow. AIChE J., vol. 22, no. 1, 1976, p. 47.

9. Barnea, D.: A Unified Model for Predicting Flow-Pattern Transitions for the Whole Range of Pipe Inclinations. Int. J. Multiphase Flow, vol. 13, no. 1, 1987, pp. 1–12.

10. Barnea, D.; Shoham, O.; and Taitel, Y.: Flow Pattern Transition for Vertical Downward 2 Phase Flow. Chem. Eng. Sci., vol. 37, no. 5, 1982, pp. 741–744.

11. Barnea, D.; Luninski, Y.; and Taitel, Y.: Flow Pattern in Horizontal and Vertical 2 Phase Flow in Small Diameter Pipes. Can. J. Chem. Eng., vol. 61, no. 5, 1983, pp. 617–620.

12. Munson, Bruce Roy; Young, Donald F.; and Okiishi, Theodore H.: Fundamentals of Fluid Mechanics. Third ed., John Wiley & Sons, New York, NY, 1998.

13. Wallis, Graham B.: One-Dimensional Two-Phase Flow. McGraw-Hill, New York, NY, 1969.

14. Nicholson, M.K.; Aziz, K.; and Gregory, G.A.: Intermittent 2 Phase Flow in Horizontal Pipes—Predictive Models. Can. J. Chem. Eng., vol. 56, no. 6, 1978, pp. 653–663.

15. Lin, P.Y.; and Hanratty, T.J.: Effect of Pipe Diameter on Flow Patterns for Air Water-Flow in Horizontal Pipes. Int. J. Multiphase Flow, vol. 13, no. 4, 1987, pp. 549–563.

REPORT DOCUMENTATION PAGE

1. AGENCY USE ONLY (*Leave blank*)	2. REPORT DATE December 2001	3. REPORT TYPE AND DATES COVERED Technical Paper

4. TITLE AND SUBTITLE

Near-Horizontal, Two-Phase Flow Patterns of Nitrogen and Hydrogen at Low Mass and Heat Flux

5. FUNDING NUMBERS

WU–718–90–00–00

6. AUTHOR(S)

Neil T. Van Dresar and James D. Siegwarth

7. PERFORMING ORGANIZATION NAME(S) AND ADDRESS(ES)

National Aeronautics and Space Administration
John H. Glenn Research Center at Lewis Field
Cleveland, Ohio 44135–3191

8. PERFORMING ORGANIZATION REPORT NUMBER

E–12435

9. SPONSORING/MONITORING AGENCY NAME(S) AND ADDRESS(ES)

National Aeronautics and Space Administration
Washington, DC 20546–0001

10. SPONSORING/MONITORING AGENCY REPORT NUMBER

NASA TP—2001-210380

11. SUPPLEMENTARY NOTES

Video clips of selected flow pattern samples are stored on the compact disk that accompanies this report. Neil T. Van Dresar, NASA Glenn Research Center, and James D. Siegwarth, National Institute of Standards and Technology, Boulder, Colorado 80303. Responsible person, Neil T. Van Dresar, organization code 5870, 216–977–7533.

12a. DISTRIBUTION/AVAILABILITY STATEMENT

Unclassified - Unlimited
Subject Categories: 34 and 28   Distribution: Standard

Available electronically at http://gltrs.grc.nasa.gov/GLTRS

This publication is available from the NASA Center for AeroSpace Information, 301–621–0390.

12b. DISTRIBUTION CODE

13. ABSTRACT *(Maximum 200 words)*

Experiments were conducted to obtain data on the two-phase (liquid and vapor) flow behavior of cryogenic nitrogen and hydrogen under low mass and heat flux conditions. Tests were performed in normal gravity with a 1.5° upflow configuration. Viewports in the apparatus permitted visual observation of the two-phase flow patterns. Computer codes to predict flow patterns were developed from theoretical/empirical models reported in the literature. Predictions from the computer codes were compared with experimental flow pattern observations. Results are presented employing the traditional two-dimensional flow pattern map format using the liquid and gas superficial velocities as coordinates. In general, the agreement between the experimental results and the analytical predictive methods is reasonably good. Small regions of the flow pattern maps are identified where the models are deficient as a result of neglecting phase-change phenomena. Certain regions of the maps were beyond the range of the experiments and could not be completely validated. Areas that could benefit from further work include modeling of the transition from separated flow, collection of additional data in the bubble and annular flow regimes, and collection of experimental data at other inclination angles, tube diameters, and higher heat flux.

14. SUBJECT TERMS

Two-phase flow; Flow pattern; Flow regime; Cryogenic; Nitrogen; Hydrogen

15. NUMBER OF PAGES
36

16. PRICE CODE

17. SECURITY CLASSIFICATION OF REPORT	18. SECURITY CLASSIFICATION OF THIS PAGE	19. SECURITY CLASSIFICATION OF ABSTRACT	20. LIMITATION OF ABSTRACT
Unclassified	Unclassified	Unclassified	